International Journal of Biological Sciences and Applications
2014; 1(3): 90-112
Published online September 20, 2014 (http://www.aascit.org/journal/ijbsa)

Keywords
Actin,
All-Atom Computational Analyses,
Coarse-Grained Computational Analyses,
Molecular Dynamics

Received: August 28, 2014
Revised: September 02, 2014
Accepted: September 03, 2014

Molecular and meso-scale computational analyses of microstructure and behavior of actin monomers, trimers and polymers

Angela Grujicic[1], Mica Grujicic[2, *], Ramin Yavari[2], Jennifer Snipes[2], Subrahmanian Ramaswami[2]

[1]Department of Bioengineering, Clemson University, Clemson SC 29634, USA
[2]Department of Mechanical Engineering, Clemson University, Clemson SC 29634, USA

Email address
gmica@clemson.edu (M. Grujicic)

Citation
Angela Grujicic, Mica Grujicic, Ramin Yavari, Jennifer Snipes, Subrahmanian Ramaswami. Molecular and Meso-Scale Computational Analyses of Microstructure and Behavior of Actin Monomers, Trimers and Polymers. *International Journal of Biological Sciences and Applications.* Vol. 1, No. 3, 2014, pp. 90-112.

Abstract
This paper deals with the study of microstructure and properties in actin monomers and polymers using advanced computational methods and tools. Specific aspects of actin microstructure and properties include: topological stability, DNase I-binding (DB) loop conformation, G-actin flatness, conformation of nucleotide-binding cleft, rate of ATP hydrolysis, filament persistence-length, filament bending stiffness and axial stiffness, and actin-material elastic-stiffness matrix/moduli. These actin microstructural and property aspects are investigated using a combination of all-atom and coarse-grained molecular-level computational methods, and various coarse-graining and trajectory-data post-processing procedures. Wherever possible, the results obtained are compared with their experimental counterparts in order to validate the computational approach used. Also, by comparing the all-atom and the corresponding coarse-grained simulation results, it has been established that, for the most part, coarse-grained force-field functions derived are of sufficient accuracy/fidelity to yield reasonable data regarding actin microstructure and properties.

1. Introduction

Within the present work, microstructure and properties in actin monomers and polymers are investigated using advanced computational methods and tools. Thus, the main aspects of the present work include: (a) basics of actin monomers and polymers; and (b) advanced computational methods and tools used in the study of large biological molecules such as actin. A brief overview of these aspects of the problem at hand is presented in the remainder of this section.

1.1. Basics of Actin Monomers and Polymers

Actin is a protein which exists within eukaryotic cells (cells containing organelles enclosed by lipid bilayers/membranes) in two main forms: (a) as a monomeric, globular G-actin; and (b) as a filamentous F-actin. The latter is formed by self-assembly/polymerization of G-actins under physiological salt concentration

conditions. G-actin is a single polypeptide chain consisting of 375 amino acid residues and has a molecular weight of about 43 kDa (1 Da is one-twelfth the mass of an atom of carbon- 12). While monomeric G-actin is bound to one molecule of adenosine tri-phosphate (ATP) and one calcium ion, hydrolysis of ATP (severing one of the phosphate bonds through interaction with a water molecule) during actin polymerization produces adenosine di-phosphate (ADP) and an inorganic phosphate ion, and the ADP remains bound to the G-actin within the resulting polymer. A variety of factors within the cell affect the dynamic equilibrium between the monomeric and polymeric forms of actin [1]. As a result, F-actin polymeric chains behave as dynamic structures that continuously grow at one end and break up at the other end in response to the local physiological conditions/stimuli within the cell.

Actin polymers/filaments are the major components of the cellular cytoskeleton, and they also play critical roles in numerous processes in eukaryotic cells, such as: (i) cell motility/mobility; (ii) cytokinesis (i.e. a process in which the cytoplasm of a single eukaryotic cell is divided to form two daughter cells); (iii) endocytosis (i.e. engulfing and absorption of proteins by cells); (iv) cell shape and polarity; and (v) intracellular mass transport [2–5]. In addition, actin filaments act as key structural elements conferring/controlling the mechanical properties of muscle tissue [6].

When analyzing microstructure/conformation of G-actin monomers, it is convenient to divide a single G-actin into four subdomains. Following Holmes et al. [7], the four subdomains (D*n*, *n* = 1–4) are defined in the following way: D1 includes amino-acid residues 1–32, 70–144, and 338–375; D2 includes residues 33–69; D3 includes residues 145–180 and 270–337; and D4 includes residues 181–269. During this division, the adenosine group of ATP and ADP is generally assigned to D3, while the phosphate groups are generally assigned to D1. The four subdomains are colored respectively as red, cyan, yellow and orange in Figures 1(a)–(d).

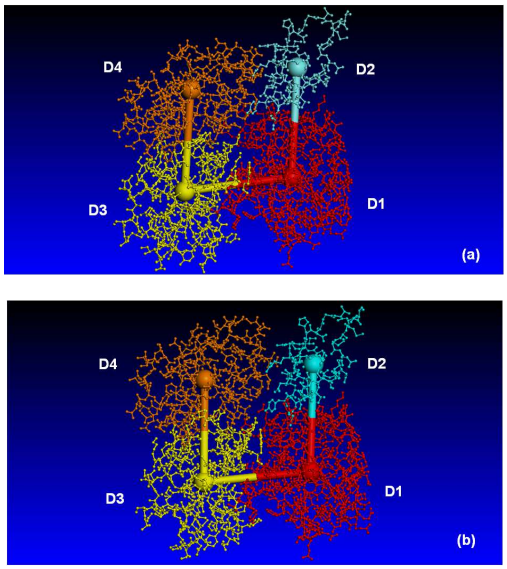

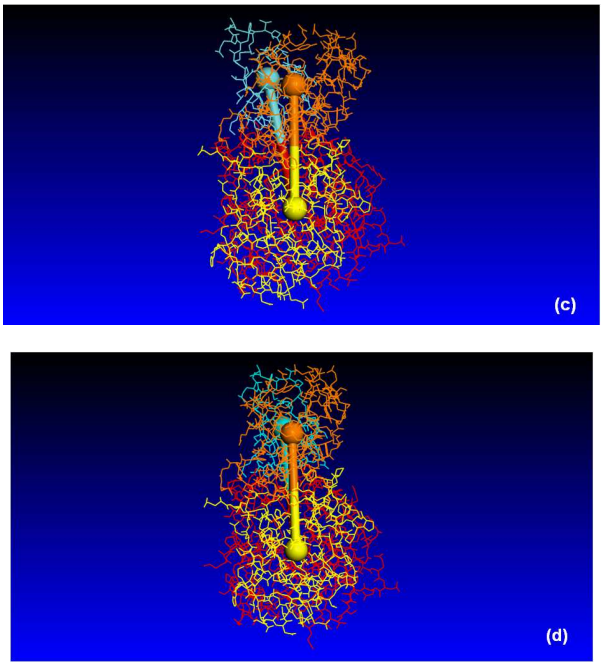

Figure 1. *Partitioning of a single G-actin into four subdomains and large-ball/large-stick coarse-grained representation of the four-bead G-actin model: (a) and (c) denote ATP-bound G-actin conformation characterized by a larger dihedral angle of the four-bead model; (b) and (d) denote ADP-bound G-actin conformation characterized by a smaller dihedral angle of the four-bead model.*

While both G- and F-actins strongly bind ATP, the rate of ATP hydrolysis is greatly different in the two cases. Specifically, the G-actin-bound ATP hydrolyses about 40,000 times slower [8, 9]. This suggests that freshly-polymerized F-actin may contain a large fraction of unhydrolyzed ATP. Various experimental (e.g. [10]) and computational (e.g. [11–13]) investigations suggested that the cause of this difference is the associated polymerization-induced changes in the nucleotide (i.e. ATP or ADP) binding cleft (defined later). However, the mechanism by which changes in the conformation of nucleotide-binding cleft affect the rate of ATP hydrolysis remains elusive (e.g. [10]). Among the noteworthy efforts aimed at resolving this problem is the work of Oda et al. [14] who suggested that polymerization-induced flattening of G-actins moves residue Q137 (glutamine) closer to the γ-phosphate group of the bound ATP. Since experimental investigations involving crystallized G-actins [15, 16] revealed that Q137 coordinates a water molecule, Oda et al. [14] suggested that actin-polymerization-induced proximity of the water molecule to the γ-phosphate group of the bound ATP may be responsible for the increased F-actin-bound ATP-hydrolysis rate. Figures 1(a)–(d) depict the aforementioned polymerization-induced flattening of the G-actin. Specifically, pre-polymerization conformation of the G-actin is depicted in Figures 1(a) and (c) while post-polymerization conformation is depicted in Figures 1(b) and (d). To highlight the polymerization-induced flattening of the G-actin, each subdomain is also represented by a

spherical bead located at the subdomain center of mass. Examination of the results displayed in Figures 1(a)–(d) reveals that the dihedral angle formed by the D2-D1-D3-D4 bead chain decreases during polymerization, giving rise to G-actin flattening.

Various investigations (e.g. [14, 17]) have established that F-actins possess an ordered (i.e. crystalline) structure consisting of 13 G-actin unit cells. An example of the F-actin unit cell is depicted in Figure 2(a). To form an infinitely long F-actin filament, the unit cell is continuously replicated in the longitudinal (i.e. along the filament axis) direction. A simplified version of the F-actin structure in which each G-actin subdomain is replaced by the corresponding spherical bead (located at the center of mass of the subdomain) is depicted in Figure 2(b). As shown in Figures 2(c) and 2(d), the arrangement of the G-actins within a single F-actin unit cell could be described either using a single left-handed short-pitch helical structure (six turns per unit cell) or two right-handed large-pitch helices (one-half of the turn per unit cell, for each helix). In Figures 2(c)–(d), each G-actin (rather than each G-actin subdomain) is represented by a spherical bead (located at the G-actin center of mass). Two bead colors are used in these figures to help distinguish between the two right-handed helical arrangements.

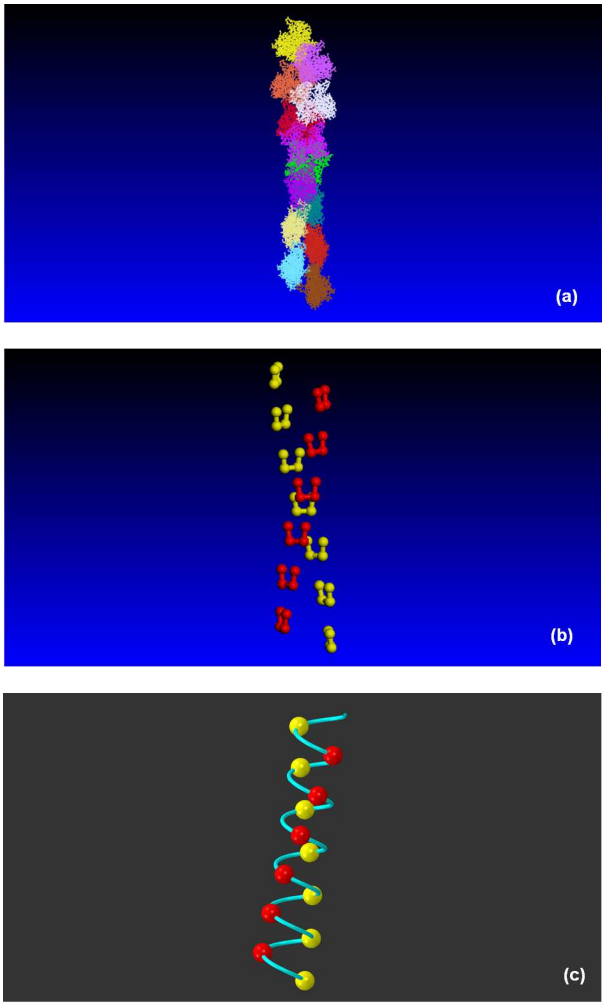

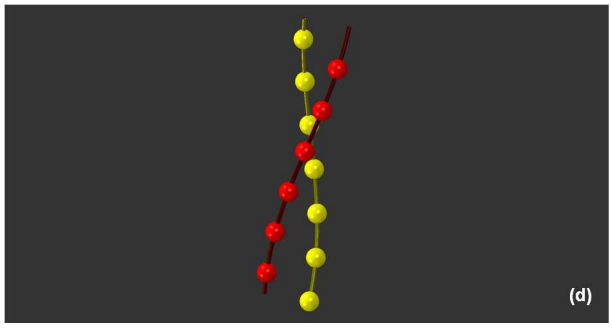

Figure 2. *(a) All-atom representation of a 13-G-actin unit cell of an F-actin filament; (b) Same as (a), except that each G-actin is represented by the four-bead coarse-grained structure; (c) Schematic representation of the F-actin structure as a single left-handed short-pitch helix; and (d) Schematic representation of the F-actin structure as two right-handed long-pitch helices.*

Currently, there are two widely-recognized F-actin structural models: (a) the so-called Holmes model [17]; and (b) the so-called Oda model [14]. While both models are based on the helical arrangement of 13 G-actins within a single F-actin unit cell, the Holmes model assumes the structure of G-actins to be that displayed in Figures 1(a) and (c), and, thus, to remain effectively unchanged upon polymerization. On the other hand, within the Oda model, the aforementioned flattening of G-actins is included in the construction of the F-actin unit cell. Consequently, G-actin conformation within the Oda model is that displayed in Figures 1(b) and (d).

Another conformational change accompanying polymerization of G-actin monomers into an F-actin polymer is the change in conformation of DNase I-binding (DB) loop, a loop that is composed of amino-acid residues 40–48, located in subdomain 2. The DB loop binds DNase I, an enzyme responsible for cleaving DNA molecules. When DNase I is bound to the actin monomer or polymer, the enzyme is rendered inactive. It is well-established that in the case of ATP-bound G-actins, the DB loop adopts a "*loop-type*" conformation [e.g. 17]. However, upon ATP hydrolysis, the DB loop acquires a secondary structure corresponding to an α-helix [e.g. 14]. In Figures 3(a)–(d), zoomed-out, Figures 3(a)–(b), and zoomed-in, Figures 3(c)–(d), all-atom configurations of a G-actin (hydrogen atoms are not displayed, for clarity) for the two conformations of the DB loop are shown. In Figures 3(a) and (c), the "*loop conformation*" is displayed while in Figures 3(b) and (d), the "*helical conformation*" is depicted. For improved clarity, the α-carbon atoms of the DB loop are shown as larger cyan spheres in Figures 3(a)–(d). Experimental studies involving electron microscopy, proteolysis, and fluorescence spectroscopy [18–23] have suggested that this change in the conformation of the DB loop is related to the release of (inorganic) γ-phosphate during ATP hydrolysis. Since ATP hydrolysis and, thus, the process of γ-phosphate release, takes place at a finite rate, some G-actins within the actin polymers have been found to exhibit a loop-type [9, 16] while others have a helix-type [16] DB loop conformation. In addition, it has been

suggested that the release of the phosphate is related to an increase in susceptibility to destabilization of F-actins in the presence of actin-depolymerization proteins. This destabilization promotes filament disassembly at its "*pointed*" (non-growing) end and regulates filament growth [1, 24–25] at its "*barbed*" end.

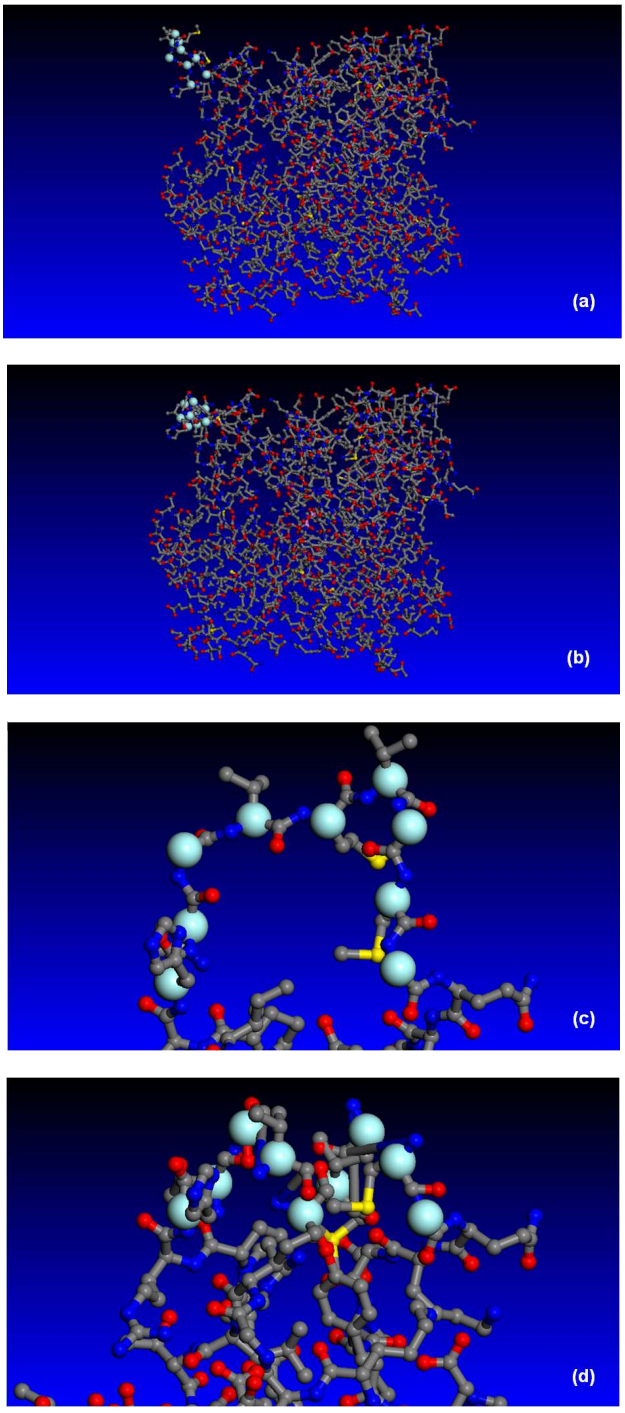

Figure 3. *Zoomed-out (a–b), and zoomed-in (c–d), all-atom configurations of a G-actin (hydrogen atoms are not displayed, for clarity). (a) and (c) display "loop conformation" while (b) and (d) display "helical conformation" of the DNase I-binding (DB) loop. For improved clarity, the α-carbon atoms of the DB loop are shown as larger cyan-colored spheres.*

1.2. Computational Investigation of Actins

Experimental techniques such as electron microscopy and X-ray diffraction commonly employed in experimental investigations of actin microstructure and properties generally suffer from limited spatial resolution which, in turn, curtails their ability to accurately quantify filament microstructure and mechanical properties as manifested by, for example, filament flexibility. To help overcome these limitations of the experimental techniques, microstructure and properties of actin monomers and polymers/filaments are also being investigated using modeling and simulation approaches. An overview of the public-domain literature carried out as part of the present work revealed that modeling and computational simulations of actins and related proteins have been carried out using a variety of numerical methods and tools. These methods/tools can be generally classified as: (a) continuum-level methods/tools, (b) all-atom molecular-level simulations; and (c) coarse-grained computational analyses. A brief overview of the past efforts employing the three classes of computational methods and tools is given below.

Conventional continuum methods based on linear and nonlinear elastic-material approximations have been used by several investigators (e.g. [2, 26–29]) to analyze mechanical properties of actin-based cytoskeleton structures. Clearly, at the fine length-scale of the actin microstructure, the continuum approximation is questionable and, hence, the results obtained may be suspect. In addition, continuum-level methods and tools are incapable of conveying the important effect of molecular-level conformation and microstructure of the composing actin filaments and ligands on the cytoskeleton mechanical response.

In contrast to the continuum-type computational methods and tools, all-atom molecular dynamics (MD) simulations are capable of revealing atomic-scale microstructural details of actin monomers and polymers [30–32]. For example, the aforementioned change in the DB loop conformation from the loop type to the α-helix type has been predicted using MD simulations [33]. In addition, the experimentally observed effect of DB-loop conformation on the structural and mechanical properties of F-actins has been validated using MD simulations involving 13 G-actin unit cells of the F-actin polymeric chains [33]. Furthermore, MD simulations can provide important insight into the processes which regulate F-actin growth/disintegration, e.g. [34, 35]. Unfortunately, despite all these advantages offered by MD simulations, these computational techniques suffer from a number of limitations which are primarily related to the limited time-scale covered by the simulations (typically less than 100 ns) and length-scale of the computational model (typically less than 50 nm). Consequently, MD simulations are not generally used to study longer actin filaments, filament growth/disintegration dynamics, or the interactions of F-actin with motor proteins such as myosin.

To address the aforementioned limitations of the MD

simulation methods, coarse-grained (c.g.), also referred to as meso-scale [e.g. 31, 36–39], methods and tools have been devised. Within the c.g. methods, some of the all-atom details have been traded for an increase in the accessible time and length scales. Provided the c.g. methods are capable of capturing the essential physics of the phenomena and processes of interest, they can be used to study larger actin-based structures and do so over a longer time scale. To ensure that the c.g. methods possess the required level of physical fidelity, they are generally derived using the corresponding all-atom models. Thus, when constructing c.g. models, a multi-scale approach is used, within which information is exchanged between atomic-level models and their coarse-grained representations [e.g. 40].

There are few c.g. models for actin-related structure reported in the open literature. In one of these models, the so-called "*Elastic Network Model*" (ENM) is utilized within which the c.g. particles (commonly referred to as beads) are connected with effective harmonic bonds with a universal force constant [41–46]. Typically, within the ENM framework, each amino-acid residue is represented by a single c.g. bead, and the bead is placed at the location of the α-carbon within the residue. The corresponding actin conformation determined using X-ray diffraction is used as the reference/equilibrium configuration for the c.g. model. Within an alternative ENM-based coarser c.g. model for actin, each G-actin is represented by a single bead [47]. This version of the F-actin c.g. model is depicted in Figures 2(c)–(d).

Due to the fact that the ENM-based c.g. models for actins utilize harmonic bonds with a universal force constant, they are generally found to be limited in predicting phenomena and processes related to the G-actin conformational changes associated with the polymerization process and with G-actin/G-actin interactions. Consequently, structural and mechanical properties of F-actins such as their flexural rigidity and persistence length (defined later) are not generally well-predicted by the ENM-based c.g. F-actin models [40]. In addition, c.g. models in which each amino-acid residue is represented by a bead, may be computationally too expensive when studying the behavior of long F-actin filaments. On the other hand, c.g. F-actin models in which each G-actin is represented by a single bead may be too coarse to account for the phenomena such as the F-actin polarity and for interactions between F-actin and actin-binding proteins.

To overcome the aforementioned limitations of the two c.g. ENM-based F-actin models, an intermediate c.g. F-actin model was introduced in Ref. [40]. Within this model, each G-actin is represented by four subdomain-related beads, Figures 1(a)–(d). Intra-G-actin interactions are modeled by three harmonic bonds, two harmonic bond angles and one harmonic dihedral angle (each having its own parameterization). In addition, inter-G-actin interactions are accounted for through the use of the (hypothetical) harmonic bonds (again, each having its own parameterization) connecting the domains of one G-actin with the domains of the adjacent G-actins within the actin polymer. The intermediate c.g. F-actin model has been validated by comparing its predictions with the all-atom MD simulation and experimental counterparts [40]. This validation established that the intermediate c.g. F-actin model provides a good compromise between physical fidelity and computational efficiency [40].

1.3. Main Objectives

The main objective of the present work is to carry out a comprehensive computational investigation involving both all-atom and coarse-grained methods in order to determine and quantify various aspects of the G-actin monomer, actin-trimer and actin-polymer conformation/microstructure and properties while, as the literature review presented in the previous sections reveals, there are several reports dealing with various aspects of actin microstructure and properties, a comprehensive multi-scale investigation of this problem is still lacking.

1.4. Paper Organization

Sections 2.1–2.2 contain, respectively, a brief description of the all-atom molecular-level and coarse-grained meso-scale computational methods and tools used in the present work. Post-processing methods employed to determine/quantify various aspects of the actin conformation/microstructure and properties are overviewed in Section 2.3. A statement of the problem analyzed in the present work is given in Section 2.4. An overview and discussion of the main results obtained are given in Section 3. Key conclusions resulting from the present work are summarized in Section 4.

2. Computational Analyses

In the present work, various aspects of actin monomer, trimer and polymer/filament microstructure and properties are investigated using all-atom molecular-level and meso-scale (i.e. coarse-grained) computational methods and tools. These methods and tools consider a material as a system of interacting (including bonded) discrete particles (i.e. atoms or ions within the all-atom framework and assemblies of particles, called beads, within the coarse-grained computational framework) and utilize potential-energy minimization based (molecular statics) and/or Newton's second law based (molecular dynamics) algorithms to examine and quantify the behavior and properties of the subject structure/material. It is generally recognized that computational methods and tools which are based on a combination of molecular-level and meso-scale approaches, provide advantages over the methods and tools which rely on the use of only one of the aforementioned approaches. Specifically, despite not being as accurate as the quantum mechanical methods (limited to material systems containing no more than a few hundred interacting particles), the all-atom molecular-level computational

methods are generally considered to be of high fidelity and applicable to the analysis of large structural/material systems (typically containing millions of particles). On the other hand, computed results based on multi-million-particle molecular-level calculations are often difficult to interpret, and coarse-graining, which involves beads (hypothetical particles which contain a large number of bonded and closely-spaced interacting atoms/ions and are expected to account accurately for the collective behavior of these atoms/ions), can be quite beneficial in regards to this matter. In addition, as mentioned earlier, the c.g. methods can be used to significantly increase the accessible time and space scales. In the remainder of this section, a brief description is provided of the key aspects of all-atom molecular-level and coarse-grained computational models and procedures employed in the present work. In addition, post-processing techniques used to determine and quantify various aspects of the actin conformation/microstructure and properties are presented in the last part of this section.

2.1. All-atom Molecular-Level Computational Analyses

In general, complete definition of a molecular-level computational model and analysis requires specification of: (a) geometrical (e.g. atomic positions, computational cell size, etc.) and chemical (e.g. atomic species, bond order, etc.) details of the computational model; (b) a set of fully parameterized force-field functions (inter-atomic potentials); and (c) details regarding the type, the number and the usage sequence of the molecular-level computational algorithms/methods to be used in the simulation. More details of these three aspects of the present computational effort are presented in the remainder of this section.

2.1.1. Molecular-level Computational Models

Systems Analyzed: All-atom molecular-level calculations carried out in the present work involved six different actin configurations. These included two distinct (i.e. ATP-bound and ADP-bound) configurations for three types (i.e. G-actin monomers, actin trimers and F-actin polymers) of actin-based assemblies. Construction and visualization of the molecular-level models for the six actin-based systems (described below) was carried out using Visualizer program from Accelrys [48] in combination with MATLAB, a general-purpose mathematical package [49]. G-ATP and G-ADP configurations of each actin assembly are analyzed in order to examine the effect of ATP-hydrolysis-induced changes in the DB loop conformation on the actin structure and behavior.

G-actins are analyzed because they are the basic building blocks of F-actin polymers and undergo topological changes during self-assembly/polymerization. All-atom models of the two (ATP-bound and ADP-bound) conformations of the G-actin analyzed in the present work have already been shown in Figures 1(a), (c) and in Figures 1(b), (d), respectively.

Trimers are generally studied because they represent the basic F-actin nucleus which contains all essential intra- and inter-G-actin interactions present in the F-actin polymer. In the present work, they are mainly used to test the physical soundness of the G-actin monomer and actin polymer results. An example of an all-atom model for the (ATP-bound) actin trimer analyzed in the present work is shown in Figure 4(a).

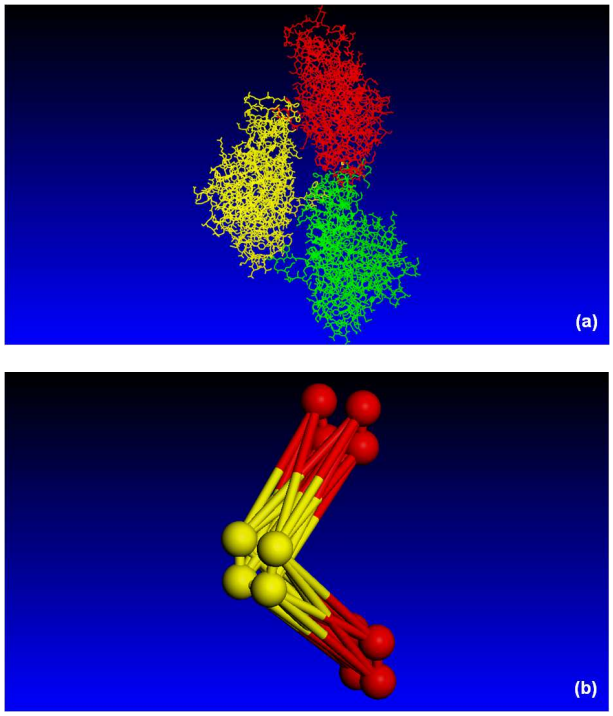

Figure 4. *(a) All-atom; and (b) coarse-grained models for actin trimers analyzed in the present work.*

F-actin polymers are investigated because they are one of the major components of the cytoskeleton. An example of the all-atom model for the F-actin polymer analyzed in the present work has already been shown in Figure 2(a).

G-actin Models: The molecular-level models for the ATP-bound G-actin (G-ATP), 1NWK [15], and the ADP-bound G-actin (G-ADP), 1J6Z [16], are taken from the Protein Data Bank (PDB) [50]. Each G-actin contains 375 residues and 5,838 atoms, not counting the atoms associated with ATP or ADP or additional atoms associated with post-translational chemical modifications of actin (acetylation of the N-terminal aspartate or methylation of HIS73). It should be noted that the original 1NWK G-ATP model is missing atomic coordinates for residues 1–5, 40–51, and 372–375. Also, the original 1J6Z G-ADP model is missing atomic coordinates for residues 1–3 and 373–375, along with some atomic coordinates in residue 4. All the missing coordinates were generated by importing the corresponding coordinates from the 1ATN G-ATP model of Holmes et al. [7] while maintaining the internal coordinates (i.e. coordinates defined with respect to the computational unit cell, defined later) unchanged. The resulting all-atom

molecular-level models for the ATP-bound and ADP-bound G-actin configurations are shown in Figures 1(a), (c), and 1(b), (d), respectively. Before solvation (i.e. immersion in water), the two G-actin configurations are found to fit into a 7.3 nm × 6.6 nm × 4.0 nm rectangular parallelepiped-shaped box.

Actin Trimer and Polymer Models: Since similar procedures are used to construct actin trimer and actin filament all-atom models, these procedures are explained in the same, the present, section. To generate the molecular-level models for ATP- and ADP-bound actin trimers and F-actin polymers, the corresponding G-actin molecular-level models are replicated and rearranged in accordance with the F-actin model proposed by Holmes et al. [17]. This model was shown in Figure 2(c). As mentioned earlier, within this model, thirteen G-actins are positioned over a repeat distance of ca. 35.75 nm along the F-actin polymer axis as a left-handed, short-pitch, six-turn helix. Following this model, to construct actin trimer and polymer models, each subsequent G-actin is rotated by 166° (= 12/13 × 180°) about and translated (in a left-hand sense) by 2.75 nm along the helix axis towards the barbed/growing end of the polymer. The actin trimer model is then constructed by placing 3 G-actins while the F-actin model is constructed by placing 13 G-actins within a single repeat distance along the helix axis. An example of the resulting 13-G-actin model for F-actin polymer is depicted in Figure 2(a), while an example of the resulting actin trimer model is depicted in Figure 4(a). The actin-trimer and F-actin repeat units (both in their ATP-bound and ADP-bound configurations), before solvation, are found to respectively fit into 9.8 nm × 9.8 nm × 10.3 nm and 9.8 nm × 9.8 nm × 35.75 nm rectangular parallelepiped-shaped boxes, with the third edge of each box being aligned with the filament axis (which, in turn, is aligned with the *z*-coordinate axis).

Solvation, Neutralization and Physiological Concentration Adjustment: To model the behavior of actins under physiological conditions within a cell, all six actin systems analyzed are solvated explicitly by surrounding them with water molecules (represented with the TIP3P model [51]), with at least four solvation shells from each actin system to each lateral face of the computational unit cell. To mimic the hydration process (i.e. the interaction between water molecules and actin moieties) more closely, while adding water molecules, care was taken to ensure that no oxygen atom of a water molecule is placed closer than 0.24 nm to the heavy atoms of protein molecules (or to the ions, discussed below). Since G-actins possess a negative charge of –10 (a balance of negative charge induced by ionization of ASP and GLU residues and positive charge induced by singly protonated HIS residues), neutralizing ions are added to the system by replacing some of the previously added water molecules with K^+. In addition, counter K^+ and Cl^- ions are added to the system, by replacing water molecules, in order to attain the physiological concentration of KCl of 140 mM.

Periodic Boundary Conditions: All models analyzed employed the use of a computational unit cell in order to enforce periodic boundary conditions across all faces of the computational cells. The three edges of the unit cell in each model are aligned respectively with the three coordinate axes. In the case of G-actins, actin trimers and lateral directions of the F-actins, the dimensions of the unit cell are dictated by the imposed four solvation shells condition. On the other hand, in the case of F-actins, the unit cell in the longitudinal direction is controlled by the periodicity of the F-actin molecular structure in this direction.

Model Summary: A summary of the basic constituents and geometrical aspects of the six actin-based all-atom molecular-level models is given in Table 1.

Table 1. *Basic constituents and unit cell sizes for the six (ATP-bound and ADP-bound) conformations of actin monomers (G), actin trimers (T), and actin filaments (F). [33]*

	G-ATP	**G-ADP**	**T-ATP**	**T-ADP**	**F-ATP**	**F-ADP**
Protein atoms	5,881	5,874	17,643	17,631	76,453	76,401
Ca^{2+} ions	4	6	10	16	39	65
K^+ ions	36	30	87	73	332	273
Cl^- ions	30	29	65	66	228	234
Water molecules	19,649	19,651	51,164	51,167	166,283	166,305
Total atoms	64,898	64,892	171,297	171,287	575,901	575,888
Unit cell size x×y×z, nm	9.6×7.3×9.3	9.6×7.3×9.3	12.7×9.2×14.6	12.7×9.2×14.6	12.5×12.5×36.6	12.6×12.6×35.6

2.1.2. Molecular-Level Force-Fields

It is well recognized that the overall utility of molecular-level computational analyses is highly affected by fidelity and accuracy of the employed force-fields (a set of mathematical expressions which quantify the contribution of various bonding and non-bonding interactions between the constituents of the molecular-scale model to the material-system potential energy). It is generally found that the force-field functions can greatly affect not only the potential energy of a material system but also its microstructure, properties and temporal behavior/evolution (including structural/morphological stability).

In the present work, the so-called GROMOS96 force-field functions [52] were utilized to characterize intra-actin and intra-nucleotide (ATP or ADP) bonding interactions. Within the GROMOS96 force-field [52], the potential energy of a system of bonded and interacting particles is

expressed as a sum of: (a) the valence (or bond), $E_{valence}$; (b) the cross-term, $E_{cross\text{-}term}$; and (c) the non-bond, $E_{non\text{-}bond}$, interaction energies as:

$$E_{total} = E_{valence} + E_{cross-term} + E_{non-bond} \tag{1}$$

The valence energy, in turn, contains the following components: (a) a bond stretching term, E_{bond}; (b) a two-bond included-angle term, E_{angle}; (c) a three-bond-dihedral-torsion term, $E_{torsion}$; (d) an inversion (or a four-atom out-of-plane interaction) term, E_{oop}; and (e) a Urey-Bradley term (involves interactions between two atoms bonded to a common atom), E_{UB}, as:

$$E_{valence} = E_{bond} + E_{angle} + E_{torsion} + E_{oop} + E_{UB} \tag{2}$$

The cross-term interacting energy, $E_{cross\text{-}term}$, accounts for the interaction of various valence components of the potential energy and includes interaction energies involving: (a) stretch-stretch interactions between two adjacent bonds, $E_{bond\text{-}bond}$; (b) stretch-bend interactions between a two-bond angle and one of its bonds, $E_{bond\text{-}angle}$; (c) bend-bend interactions between two valence angles associated with a common vertex atom, $E_{angle\text{-}angle}$; (d) stretch-torsion interactions between a dihedral angle and one of its end bonds, $E_{end\_bond\text{-}torsion}$; (e) stretch-torsion interactions between a dihedral angle and its middle bond, $E_{middle\_bond\text{-}torsion}$; (f) bend-torsion interactions between a dihedral angle and one of its valence angles, $E_{angle\text{-}torsion}$; and (g) bend-bend-torsion interactions between a dihedral angle and its two valence angles, $E_{angle\text{-}angle\text{-}torsion}$, terms as:

$$\begin{aligned} E_{cross-term} = {} & E_{bond-bond} + E_{angle-angle} + E_{bond-angle} + E_{end\_bond-torsion} + E_{middle\_bond-torsion} \\ & + E_{angle-torsion} + E_{angle-angle-torsion} \end{aligned} \tag{3}$$

The non-bond interaction term, $E_{non\text{-}bond}$, accounts for the interactions between non-bonded atoms and includes: (a) the van der Waals energy, E_{vdW}; and (b) the Coulomb electrostatic energy, $E_{Coulomb}$, as:

$$E_{non-bond} = E_{vdW} + E_{Coulomb} \tag{4}$$

It should be noted that the Coulomb term includes hydrogen bonding interactions.

Analytical expressions for various bond and non-bond interaction energies appearing in Eqs. (1)–(4), as used by the GROMOS96 force-field functions, can be found in Ref. [52]. It should be noted that GROMOS96 is a reactive type of force-field potential since it enables adaptive formation and breaking of the inter-atomic bonds.

It is generally recognized that the computation of non-bond interaction terms can be quite costly since it involves a summation over a large number of interacting atoms/ions. This problem is particularly evident in the case of large biomolecules such as the present case. To reduce the computational cost of non-bond interactions involving atoms and ions of G-actins, water molecules and salts, the all-atom approach which considers explicit interaction between all particle pairs involved is not used. Instead, the long-range van der Waals and electrostatic interactions were computed by the particle mesh Ewald algorithm [53]. Within this algorithm, summation of the non-bond energy interactions within the real space is replaced, within the periodic systems, by the corresponding summation over the Fourier space, taking advantage of the resulting high rate of convergence.

2.1.3. Molecular-Level Computational Methods and Procedure

All molecular-level calculations are carried out using GROMACS computer program [54]. In these calculations, two types of computational methods are employed: (a) molecular statics (MS); and (b) molecular dynamics (MD).

Molecular Statics: The molecular statics method is essentially an optimization technique within which the potential energy (objective function) of the computational cell is minimized with respect to the positions of the constituent atoms (design variables). The potential energy minimization within GROMACS [54] is conducted by adaptively engaging and disengaging the Steepest Descent, Conjugate Gradient and the Newton's minimization algorithms. That is, the Steepest Descent method is employed in the earliest stages of the minimization procedure in order to efficiently arrive at a molecular-level configuration which is quite close to its optimum counterpart (i.e. the one associated with the minimum potential energy). On the other hand, in the latest stages of the minimization procedure, the Newton's algorithm is employed which ensures a monotonic and stable evolution of the material into its optimal configuration.

Molecular Dynamics: Within the molecular dynamics method, negative gradient of the potential energy evaluated at the location of each atom/ion is first used to compute forces acting on each atom/ion. Then, the associated Newton's equations of motion (three equations for each atom/ion) are integrated numerically with respect to time in order to determine the temporal evolution of the material molecular-level configuration. Molecular dynamics methods are generally classified into the equilibrium and non-equilibrium methods. Within the equilibrium molecular-dynamics methods, the subject material system is maintained in the state of thermo-mechanical equilibrium by coupling it to the surroundings, such as a constant-pressure bath, a constant-temperature reservoir, etc. This ensures the absence of net fluxes of the mass, momentum and energy in any of the three principal coordinate directions. Within non-equilibrium molecular dynamics, on the other hand, the system is subjected to large mechanical and/or thermal perturbations. As a consequence, the system experiences large fluxes of its thermodynamic quantities

(mass, momentum and energy).

In the present work, only the *NPT* equilibrium molecular dynamics method was used where *N* represents a (fixed) number of atoms/ions, *P*, the hydrostatic pressure (fixed at 1 atm), and *T*, the absolute temperature (fixed at a body temperature of 310 K). Within the molecular-dynamics simulations, particle equations of motion are integrated using the Verlet/leapfrog algorithm [55]. In order to reduce the computational cost, the SHAKE algorithm [56] was used to constrain the lengths of all bonds involving hydrogen.

Computational Procedure: Typically, the following sequence of molecular-level computational analyses was employed in the present work: (a) a dynamic equilibration procedure is first employed by assigning atoms/ions velocities consistent with (the normal body temperature of) T = 310 K and by employing a velocity quenching/scaling procedure (a procedure which gradually removes the kinetic energy of the system) over a time period of ca. 40 ps. This step of the computational procedure employed ensures that the system acquires a configuration which is close to the one associated with the minimum potential energy; (b) this was followed by an energy-minimization (molecular-statics) procedure. To retain structural integrity of the actin model being analyzed, this minimization was carried out under the condition that C_α atoms of all actin residues remained fixed; (c) the system is next reheated (while running molecular-dynamics simulations), using the particle-velocity-assignment algorithm, to T = 310 K at a heating rate of 31 K/ps while still restraining the motion of the C_α atoms; (d) a 40-ps dynamic equilibration employing velocity scaling is next used while the restraints imposed on the C_α are gradually relaxed; and (e) finally, a data-generation step is carried out using NPT molecular-dynamics simulations without constraints imposed on the C_α atoms. In these simulations, a Langevin thermostat with a damping coefficient of 0.5 ps^{-1} was used to maintain the system temperature at 310 K while a Langevin-piston barostat [23] was used to maintain pressure at 1 atm.

The computational procedure described above yielded trajectory results consisting of particle positions, velocities and forces at different times during the simulation run. As discussed in greater detail in Section 2.3, these results are analyzed in order to extract and quantify actin conformation/microstructure and properties, using a combination of post-processing capabilities of GROMACS [54], Discover molecular-dynamics program from Accelrys [57] and a series of in-house-developed computer programs implemented in MATLAB [49].

2.2. Coarse-Grained/Meso-Scale Computational Analyses

As in the case of the all-atom molecular-level calculations, the complete definition of a meso-scale computational model and analysis requires specification of: (a) geometrical (e.g. bead coordinates, computational cell size, etc.) and chemical (e.g. bead type, bond order, etc.) details of the computational model; (b) a set of fully parameterized meso-scale force-field functions; and (c) details regarding the type, the number and the usage sequence of the meso-scale computational algorithms/methods to be used in the simulation. More details of these three aspects of the present coarse-grained computational effort are presented in the remainder of this section.

2.2.1. Meso-Scale Computational Models

Coarse-graining of the all-atom molecular-level models has been carried out at the levels of G-actin monomers and F-actin polymers. Details of these two coarse-graining procedures are described below.

G-actin Monomer Coarse-Grained Model: Coarse-graining of individual G-actin monomers has been used in order to help elucidate the characteristics of G-actin flexibility. Coarse-graining of a single G-actin is carried out by assigning a single bead to each of the four G-actin sub-domains as defined by Holmes et al. [7]. In accordance with the common practice, the adenosine group of ATP/ADP was assumed to belong to sub-domain 3 while the phosphate groups were assigned to sub-domain 1. The mass and location of each bead correspond to the sub-domain mass and center of mass, respectively.

As mentioned earlier, a ball-stick representation of the four-bead coarse-grained structure of a single G-actin along with its all-atom representation in which different sub-domains are assigned different colors is displayed in Figures 1(a)–(d). Examination of Figures 1(a)–(d) reveals that a coarse-grained G-actin contains six internal coordinates including three (D2–D1, D1–D3 and D3–D4) bonds, two (D2–D1–D3 and D1–D3–D4) bond angles, and one (D2–D1–D3–D4) dihedral angle. For each sub-domain, the reference position of the corresponding bead is set equal to the equilibrium position of the associated sub-domain center of mass. The latter is computed as the mass-weighted ensemble average of the corresponding MD simulation trajectory results.

Actin-Trimer Coarse-Grained Model: A schematic of the actin-trimer c.g. model is depicted in Figure 4(b). It should be noted that, for improved clarity, G-actins are assigned larger separation along the filament axis and the beads associated with the same right-handed large-pitch helix are given the same color. Since actin trimer is a nucleus of an actin polymer, and it contains all the essential bonding features of the longer actin-polymeric chain, the model shown in this figure can be treated as a subset of the polymer model (described below) and, hence, will not be explained in detail here.

Actin-Polymer Coarse-Grained Model: Coarse-grained models of F-actin polymers are primarily used to quantify inter-G-actin interactions and their contribution to the F-actin structure and properties. Two types of coarse-graining have been applied to F-actins: (a) within the first type of coarse-graining, each G-actin is represented in terms of the four sub-domain beads and, in addition to the six internal

coordinates mentioned earlier in conjunction with G-actin coarse-graining, additional bonds are placed between sub-domains of the neighboring G-actins within the polymeric chain. The resulting coarse-grained F-actin model is displayed in Figure 2(b). It should be noted that, for improved clarity, inter-G-actin bonds are not shown in this figure. The coarse-grained model obtained in this case is used in a series of computational simulations in order to assess microstructure and properties of F-actin polymers; and (b) within the second type of coarse-graining, each G-actin, within the polymeric chain, is represented by a single bead (located at the corresponding G-actin center of mass). As above, the reference configuration is obtained by mass-weighted ensemble-averaging of the corresponding all-atom MD simulation results. As discussed earlier, this procedure results in the formation of a two-α-helix bead structure, Figure 2(d). This type of coarse-graining is used to help interpret all-atom molecular-level computational results rather than for carrying out direct coarse-grained computational simulations. Towards that end, as will be discussed in greater detail in a subsequent section, the two-α-helix bead structure is further coarse-grained by combining the two strands into a single linear chain. As will be shown below, the resulting coarse-grained F-actin model can be used in combination with the theory of linear polymers [2, 28, 58] to determine the persistence length (a measure of the bending stiffness) of F-actin directly from the all-atom molecular dynamics simulation results.

2.2.2. Meso-Scale Force-Fields

Intra-G-actin Force-Fields: Temporal evolution of the aforementioned six internal coordinates resulting from coarse-graining of a G-actin is assumed to be controlled by the corresponding effective meso-scale force-field functions as follows: (a) harmonic functions [33] in the form

$$U_{ij} = -k_{ij}\left(r_{ij} - r_{ij}^{0}\right)^{2} \tag{5}$$

and

$$U_{ijk} = -k_{ijk}\left(\theta_{ijk} - \theta_{ijk}^{0}\right)^{2} \tag{6}$$

are used to respectively represent bond-stretch and two-bond-angle interactions; while (b) a cosine potential of multiplicity $N = 1$ [30, 31]:

$$U_{ijkl} = -U_{ijkl}^{0}\cos N\phi_{ijkl} \tag{7}$$

is used to represent three-bond dihedral-angle interactions. In Eqs. (5)–(7), the following nomenclature is used: U represents the potential energy term in question, k denotes the corresponding stiffness constant, r the bond length, θ the bond angle, and ϕ the dihedral angle, superscript 0 denotes a reference/equilibrium quantity while subscripts i, j, k, l are used to denote the four G-actin beads.

Inter-G-actin Force-Fields: As mentioned earlier, to model inter-G-actin interactions within F-actin polymers, inter-G-actin bonds are utilized. It should be noted that these bonds are of a hypothetical character, and they are used to account for the cumulative effect of short-range non-bond interactions, such as inter-G-actin attractions provided by salt bridges, as well as van der Waals and Coulomb-type interactions. These bonds are represented using the same harmonic approximation, Eq. (5), as in the case of their intra-G-actin counterparts.

C.G. Force-Field Parameterization: Parameterization of the c.g. force-field functions given by Eqs. (5)–(7) is carried out using the procedure outlined in [33] as follows:

(a) Equilibrium values of the bond lengths, bond angles and the dihedral angle were obtained by: (i) coarse-graining the all-atom MD results (obtained by applying the all-atom computational methods described in the previous section) in such a way that a single bead is assigned to each G-actin subdomain; and (ii) calculating the time-averages of the aforementioned c.g. force-field parameters (i.e. the equilibrium bond lengths, bond angles and dihedral angle); and

(b) As far as the stiffness constants appearing in Eqs. (5)–(7) are concerned, they are also determined using the all-atom MD simulation results. This was done by recognizing that the thermal fluctuations (defined below) of the bond lengths, bond angles and torsional angles can be determined by: (i) coarse-graining and post-processing all-atom MD results; and (ii) using either a c.g. normal-mode analysis of the c.g. potential energy function [59] (the method adopted in the present work) or by post-processing c.g. MD computational results (the method used, in the present work, to validate the c.g. parameterization). When the sought-after c.g. force-field stiffness constants are selected properly, the all-atom-based and the c.g.-based fluctuation data are in agreement. Hence, in order to determine the stiffness constants appearing in Eqs. (5)–(6), the following optimization procedure as proposed in Refs. [40, 59] was used. Within this procedure: (i) for a given trial set of stiffness constants and a given constant temperature condition ($T = 310$ K), normal mode analysis is used to compute the corresponding thermal fluctuations of the six internal coordinates; (ii) the resulting fluctuations are next compared with their all-atom molecular dynamics counterparts; (iii) the stiffness constants are then adjusted in accordance with the steepest gradient method until a good match is obtained between the two sets of thermal fluctuations. In this process, self-consistent iterations were performed to identify potential interdependence between the sought-after stiffness constants; and (iv) the c.g. stiffness constants obtained are then verified by carrying out c.g. MD simulations and by computing (and matching with the all-atom results) the thermal fluctuations from the results obtained.

In the force-field parameterization procedure described above, the concept of thermal fluctuations was used. Thermal (squared) fluctuations of a quantity A can be

defined as $\langle \delta A^2 \rangle = \langle (A - \langle A \rangle)^2 \rangle$, where $\langle ... \rangle$ denotes a mean-value operator.

The force-field parameterization procedure described above has been separately applied to the analysis of G-actin monomers and actin polymers/filaments. A summary of the resulting intra-G-actin c.g. force-field parameters for the case of G-actin monomers is shown in Table 2. Tables 3 and 4, on the other hand, contain respectively the resulting intra- and inter-G-actin c.g. force-field parameters for the case of actin filaments.

Examination of the results displayed in Table 2 reveals that the equilibrium value of the dihedral angle is about 5° greater in G-ADP than in G-ATP, which is in good agreement with the X-ray experimental observations [7, 16]. Since the reference values of the dihedral angle (as well as the remaining coarse-grained force-field parameters) are all derived from the all-atom MD simulation results, this finding provides some level of validation for the all-atom MD computational procedure used. It is also worth noting that while the corresponding equilibrium values for bond angles in G-ATP and G-ADP are quite comparable, according to the results presented in Table 2, the associated (bond-angle) stiffness constants are substantially higher in the case of G-ADP, suggesting that, upon polymerization, G-actins acquire a higher level of stiffness.

Table 2. *Coarse-grained intra-G-actin force-field parameters for G-actin monomers.*

Internal Coordinates	**Bond stiffness, *k*, kcal/mol per nm^2**		**Equilibrium length, *r*, nm**	
	G-ATP	**G-ADP**	**G-ATP**	**G-ADP**
D2–D1 bond	94±29	216±68	2.56±0.01	2.63±0.008
D1–D3 bond	406±128	473±110	2.56±0.005	2.56±0.003
D3–D4 bond	826±260	672±210	2.44±0.003	2.48±0.004
	Angle stiffness, *k*, kcal/mol per rad^2		Equilibrium angle, degrees	
	G-ATP	G-ADP	G-ATP	G-ADP
D1–D3–D4 angle	895.4±245	1136.5±250	93.3±0.15	91.1±0.1
D2–D1–D3 angle	228.4±72	447.8±98	95.9±0.4	95.9±0.2
	Dihedral angle stiffness, *k*, kcal/mol		Equilibrium dihedral angle, degrees	
	G-ATP	G-ADP	G-ATP	G-ADP
D2–D1–D3–D4 dihedral angle	400.5±126	132.1±46	152.7±0.32	157.1±1.25

Table 3. *Coarse-grained intra-G-actin force-field parameters for actin filaments.*

Internal coordinate	**Bond stiffness, *k*, kcal/mol per nm^2**		**Equilibrium length, nm**	
	F-ATP	**F-ADP**	**F-ATP**	**F-ADP**
D2–D1 bond	205±70	412±214	2.623±0.059	2.585±0.044
D1–D3 bond	601±126	703±203	2.580±0.038	2.577±0.029
D3–D4 bond	645±167	864±195	2.470±0.033	2.467±0.024
	Angle stiffness, *k*, kcal/mol per rad^2		Equilibrium angle, degrees	
	F-ATP	F-ADP	F-ATP	F-ADP
D1–D3–D4 angle	881.16±299.54	926.62±435.51	92.20±2.14	91.78±2.01
D2–D1–D3 angle	697.03±257.89	599.12±285.00	92.20±2.69	94.93±3.24
	Dihedral angle stiffness, *k*, kcal/mol		Equilibrium dihedral angle, degrees	
	F-ATP	F-ADP	F-ATP	F-ADP
D2–D1–D3–D4 dihedral angle	554.76±190.28	477.25±233.73	154.48±3.80	155.89±3.63

As mentioned earlier, Table 3, like Table 2, contains intra-G-actin c.g. force-field parameters but for the case of actin filaments. A comparison of the results for the D2–D1–D3 angle stiffness parameter listed in Tables 2 and 3 shows that in the case of the actin filaments, this stiffness parameter is higher by a factor of 2–3. This finding can be related to the fact that the DB loop (located within D2) controls the contact between the adjacent G-actins (each associated with a different right-handed large-pitch helix) and, thus, lowers the fluctuation in and increases the stiffness parameter of the D2–D1–D3 angle. It should be also noted that increased stiffness of the D2–D1–D3 angular internal coordinates is linked with the higher ATPase activity of the G-actins in the filament than in the monomeric state.

As far as Table 4 is concerned, it should be noted that the following nomenclature was used for G-actin beads: *m*D*n*, where *m* is the G-actin index while *n* is the sub-domain number. It should also be noted that all G-actins along a given right-handed large-pitch helix have either an odd or

an even index.

Table 4. *Coarse-grained inter-G-actin force-field parameters for actin filaments.*

Bond type*	*k*, kcal/mol per nm^2		Equilibrium length, nm	
	F-ATP	F-ADP	F-ATP	F-ADP
1D1 – 2D1*	187.22±15.25	186.85±15.25	4.147±0.117	4.141±0.117
1D1 – 2D2	175.50±16.11	174.92±16.11	5.944±0.125	5.934±0.125
1D1 – 2D3	241.30±21.66	241.17±21.66	3.491±0.102	3.497±0.102
1D1 – 2D4	196.27±15.12	196.04±15.12	5.392±0.131	5.381±0.131
1D2 – 2D1	197.01±16.01	196.99±16.01	3.699±0.097	3.687±0.097
1D2 – 2D2	69.12±5.33	68.88±5.33	4.501±0.109	4.512±0.109
1D2 – 2D3	107.52±8.92	107.30±8.92	2.640±0.068	2.647±0.068
1D2 – 2D4	89.10±7.42	88.89±7.42	3.445±0.099	3.431±0.099
1D3 – 2D1	93.62±8.57	93.77±8.57	3.046±0.059	3.052±0.059
1D3 – 2D2	59.70±5.39	59.72±5.39	5.088±0.122	5.080±0.122
1D3 – 2D3	160.42±14.71	160.99±14.71	4.147±0.112	4.140±0.112
1D3 – 2D4	143.29±11.83	143.02±11.83	5.982±0.130	5.992±0.130
1D4 – 2D1	180.82±15.15	180.12±15.15	1.947±0.029	1.952±0.029
1D4 – 2D2	141.65±12.55	141.35±12.55	2.907±0.049	2.917±0.049
1D4 – 2D3	82.34±6.82	82.37±6.82	3.638±0.057	3.642±0.057
1D4 – 2D4	185.00±16.17	184.79±16.17	4.501±0.062	4.509±0.062

* The number in front of the subdomain label indicates the relative position of the G-actin monomer in the α-helical actin filament.

2.2.3. Coarse-Grained Computational Methods

As mentioned earlier, coarse-grained models of actin-based structures were used in two ways in the present work: (a) to carry out additional meso-scale computational analyses. In this case, the same types of computational analyses as in the molecular-level case (i.e. molecular statics and molecular dynamics) are used. However, inter-particle interactions are described using effective meso-scale force-fields in place of the molecular-level force-fields; and (b) coarse-grained structures are used to extract and help interpret various actin topological features and material properties. For example, as discussed in the next section, coarse-graining of the all-atom MD computational results is used to compute persistence length of the actin filaments, a quantity which is a measure of the F-actin intrinsic bending stiffness.

2.3. Determination of Microstructure and Properties

In this section, a brief description is provided of the post-processing computational procedures which were used to determine and quantify various microstructural characteristics and properties of actin monomers, trimers and polymers.

2.3.1. Topological Stability

Topological stability is a measure of the ability of actin filaments to retain their structural integrity in the presence of thermal fluctuations. One way of judging topological stability is by quantifying Root Mean Square Deviations (RMSDs) of the positions of all atoms within the given computational cell, as a function of time, relative to the ones in the initial/reference actin-filament structure. Clearly, the larger are the values of the RMSDs, the higher is the probability for a given actin configuration to disintegrate, i.e. the lower is its topological stability. In the present work, RMSDs are calculated as ensemble averages of the all-atom MD results pertaining to the trajectories of all α-carbon atoms (rather than all atoms) within a single F-actin unit cell. Since each G-actin contains 375 α-carbon atoms (i.e. residues) and there are 13 G-actins per actin-filament unit cell, the total number of α-carbon atoms that had to be monitored is 4,875. To arrive at a single scalar measure of the F-actin stability, the time-average of the RMSDs for the 4,875 α-carbon atoms are used in the present work.

It should be noted that the concept of RMSDs, mentioned above, is encountered frequently in the analysis of molecular dynamics trajectory data. That is, RMSDs are often used to quantify deviations of the measured/computed results from their reference levels. The deviations of the individual data points from their reference values are commonly referred to as residuals. The common procedure for calculating RMSDs involves: (i) individually squaring the residuals and summing them; (ii) dividing the sum by the number of residuals; and (iii) taking the square root of the result.

2.3.2. DNase I-Binding (DB) Loop Conformation

As mentioned earlier, polymerization of G-actins and the resulting formation of F-actins (including the concurrent ATP hydrolysis) is accompanied by the change in conformation of the DB loop from the loop-type to the helix-type. The rate at which DB loop conformational changes take place can be considered as another measure of actin topological stability. This rate is typically assessed through visual inspection of the coordinates of α-carbon atoms associated with residues 40–48, the residues which constitute the DB loop, at different stages of molecular-dynamics simulations.

2.3.3. G-actin Flatness

Flatness of G-actin monomers and G-actins within actin

polymers, which affects the conformation of the nucleotide-binding cleft (defined below), was investigated in the present work. Two different approaches, described below, are used to investigate G-actin flatness.

Within the first approach, the all-atom molecular-dynamics trajectory data were not used directly. Rather, the data for each G-actin are first coarse-grained into four beads, Figures 1(a)–(d), where the center of each bead coincides with the center of mass of the corresponding G-actin subdomain. Using this procedure for coarse-graining of the all-atom trajectory data, monomer flatness is quantified by the dihedral angle, i.e. one of the six internal coordinates of the coarse-grained G-actin. A dihedral angle of 180° corresponds to the case of a perfectly flat G-actin. To quantify the extent of G-actin flatness within actin filaments, it is a common practice to construct a probability distribution function for this dihedral angle and to examine the first few moments of this distribution function, such as: (i) first moment - mean (a measure of the average value of the quantity being investigated); (ii) second moment - standard deviation or variance (a measure of the spread of values of the quantity); (iii) third moment - skewness (a measure of the symmetry of the distribution: positive skewness denotes a distribution function with a longer/fatter right tail); and (iv) fourth moment - kurtosis (a measure of the sharpness of the distribution function about its peak, or alternatively, the breadth of the tails of this function). This approach was adopted in the present work. In addition to coarse-graining the all-atom trajectory results, coarse-grained molecular-dynamics simulations are also used to assess G-actin flatness (by determining the distribution of the dihedral angle). By comparing the dihedral-angle distribution results obtained via: (i) coarse-graining the all-atom trajectory data; and (ii) direct coarse-grained simulations, an insight was given into the quality/fidelity of the present coarse-grained force-field parameterization.

Within the second approach, G-actin flatness was investigated using all-atom MD results more directly. This was done by monitoring the backbone dihedral angles associated with residues 141/142, and with residues 336/337. The region of G-actin associated with these residues is commonly referred to as the "*hinge region*," and is frequently used to explain sub-domain rotation which is responsible for G-actin flattening [14]. The role played by backbone dihedral angles in G-actin flattening at these residues is normally examined by constructing the corresponding Ramachandran plot using the data for all G-actins within a single F-actin unit cell. The Ramachandran plot is a scatter plot of ψ vs. φ dihedral backbone angles for all the amino acid residues within the G-actin. The procedure used to define the two dihedral backbone angles involves the following steps: (i) first, within the given residue, the backbone structure is defined by the $N–C_\alpha–C$ three-atom configuration; (ii) through the peptide bonds formation with the adjacent residues, this atomic configuration is expanded into a five-atom backbone configuration in the form $C–N–C_\alpha–C–N$; and (iii) finally, the dihedral angles ψ and φ are defined by the two three-bond configurations $N–C_\alpha–C–N$ and $C–N–C_\alpha–C$, respectively. Since inter-residue peptide bonds typically result in planar ($C_\alpha–C–N–C_\alpha$) atomic configurations, the two Ramachandran angles quantify the extent of rotation of the two adjacent $N–C_\alpha–C–N$ and $C–N–C_\alpha–C$ configurations at the C_α atom of the residue of interest. It should be noted that the total rotation between the two three-bond configurations is fully defined in terms of the two Ramachandran angles because the $N–C_\alpha–C$ two-bond angle centered at the C_α of interest remains constant.

2.3.4. Conformation of Nucleotide-Binding Cleft

To a first approximation, the geometry/topology of a G-actin can be described as two lobes separated by a (nucleotide-binding) cleft. Following the general practice, conformation of the nucleotide-binding cleft is investigated in the present work by: (i) both coarse-graining each G-actin all-atom trajectory data using the four-bead c.g. model, and by carrying out a coarse-grained molecular-dynamics simulation (based on the four-bead representation of each G-actin); and (ii) monitoring the resulting internal-coordinate bond angles (D2–D1–D3 and D1–D3–D4). It is well-established that the values of these two angles control the extent of open/closed conformations of the nucleotide-binding cleft.

2.3.5. Rate of ATP Hydrolysis

One of the unresolved actin-related problems relates to the fact that the rate of ATP hydrolysis increases by four orders of magnitude during actin polymerization. It is generally recognized that glutamine-137 plays an important role in ATP hydrolysis [14]. This residue is located in the hinge region of the G-actin, the region that plays a critical role in G-actin flattening during polymerization. During the G-actin flattening process, the side chain of this residue may relocate closer to the nucleotide-binding cleft. This relocation may result in a decreased separation distance and increased binding between the residue side chain and the ATP γ-phosphate group, which, in turn, may lead to increased susceptibility to hydrolysis (i.e. a higher rate of hydrolysis) of the ATP triphosphate group relative to that observed in the case of ATP-bound actin monomers. The onset and evolution of all the aforementioned processes which are believed to be related to the ATP hydrolysis was monitored in the present work by carefully examining all-atom MD simulation results for the participating residues and functional groups. It should be noted that, since the mechanism of ATP hydrolysis involves atom-scale phenomena and processes, it could not be investigated using c.g. computational methods.

2.3.6. Filament Persistence-Length

As mentioned earlier, the persistence length of an actin filament is a (semi-quantitative) measure of the associated bending stiffness. The persistence length is a length over

which the filament of a linear type loses the correlation between positions of its backbone atoms. In other words, a stiff filament is expected to be found in configurations which are closely related to its reference (equilibrium/straight) configuration and, thus, possess a large persistence length. Conversely, compliant filaments can bend more easily and acquire configurations which are topologically quite different than their reference configurations (since the associated energy-increase is relatively small). Consequently, compliant filaments possess a small persistence length. In order to obtain a measure of the actin-filament bending-stiffness, its persistence length was determined in the present work. However, as discussed earlier, actin filaments possess an α-helical character and not a linear character, and hence, before the persistence length of actin filaments could be determined, a "*linearization*" procedure had to be devised for the actin filaments. This procedure, as well as the procedure used to determine actin-filament persistence length, is described in the remainder of this section.

The first step in the actin-filament linearization procedure involves coarse-graining of each G-actin within the actin-filament unit cell into a single bead. This is accomplished by placing a bead of the G-actin mass at the center of mass of each G-actin. As mentioned earlier, this process results in the formation of a left-handed short-pitch single-strand helix containing 13 beads, Figure 2(c). This configuration is next "*linearized*" by replacing every three adjacent G-actin beads (within the single left-handed helix) with a single bead with a position set equal to the centroid of the triangle defined by the three G-actin beads. This procedure results in a 13-bead linearized (but wavy/undulated) chain configuration that is consistent with the underlying helical symmetry of the filament. As shown below, this configuration, in conjunction with linear polymer theories [2, 28, 58] and the coarse-grained all-atom trajectory results (used to calculate G-actin-bead reference and instantaneous coordinates) can be used to determine the persistence length of F-actin.

To calculate the persistence length, L_p , the following relation was used [e.g. 28]:

$$\left\langle \cos\left(\theta(s)\right)\right\rangle = \exp\left(-\frac{s}{L_p}\right) \tag{8}$$

where s is the distance of a given point from a reference point measured along the linearized chain, θ is the angle between the linearized chain tangents at the two points, and $\langle ... \rangle$ denotes an average quantity.

Calculation of the unit tangent vector τ_i at the location of bead i is carried out using the following central differencing scheme:

$$\tau_i = \frac{r_{i+1} - r_{i-1}}{\left|r_{i+1} - r_{i-1}\right|} \tag{9}$$

where r_{i-1} and r_{i+1} are the position vectors of beads i–1 and i+1 along the linearized filament, respectively. When Eq. (9) is applied to the reference point and a non-reference point of interest, the resulting two tangent vectors can be used to calculate θ_i . As far as calculation of contour length s is concerned, a similar procedure is used to first compute the length δs_i of the contour segment associated with bead i as:

$$\delta s_i = \frac{1}{2}\left(\left|r_{i+1} - r_i\right| + \left|r_i - r_{i-1}\right|\right) \tag{10}$$

Then the associated contour length s_i is obtained by summing the segmental contour lengths between the reference bead and bead i.

It should be noted that the equilibrium configuration of the linearized F-actin chain obtained using the procedure described above is undulated/wavy while Eq. (8) assumes that such a configuration is a straight line. Consequently, while applying Eq. (8), the contribution of the linearized chain curvature to the tangent angle had to be removed. This was done using the following procedure: (i) first, the average value of the tangent vector at the location of each of the 13 beads in the equilibrium configuration is calculated; (ii) the same procedure is applied for calculating instantaneous average values of the tangent vector; and (iii) θ_i is defined as a difference between the corresponding tangent vectors obtained in (i) and (ii).

It should also be noted that due to the fact that the linearized-chain configuration repeats every 13 beads, the largest contour distance between two beads that could be analyzed is the one corresponding to the contour distance between the first and seventh beads in sequence (e.g. beads 3 and 9). Larger contour distances are not permissible since, due to the actin-filament axial periodicity, they have already been accounted for (as smaller distances). For example, the contour distance between beads 1 and 8 has already been accounted for as the contour distance between beads 8 and 1^+, where the $^+$ is used to denote the F-actin unit cell adjacent to bead 13.

Based on the discussion presented above, only six independent cos(θ) correlation functions defined by Eq. (8) can be computed. On the other hand, in these calculations, 13 independent (θ_i and s_i) pairs of values are used.

The aforementioned persistence-length calculation procedure is applied in the present work by both: (i) coarse-graining the all-atom computational results; and (ii) by directly using the results of the coarse-grained computational analysis.

2.3.7. Filament Bending Stiffness and Axial Stiffness

In the previous section, the procedure was presented for calculation of the filament persistence length. While the persistence length is a measure of the intrinsic bending stiffness of the filament, it cannot be readily converted into the actual bending stiffness. This may become a serious shortcoming in the "*structural-type*" analyses of the mechanical response of a cell in which the knowledge of

the cytoskeleton stiffness is required. In the same analyses, the knowledge of the axial stiffness (controlling extensional/compressive and buckling response) of the filaments is also required. For that reason, procedures for determination of the bending stiffness and the axial stiffness of the actin filaments are described in this section.

To calculate the bending stiffness of an actin filament, the filament is subjected to a series of uniform (and increasing magnitude) curvature bending tests (in which the filament axis is treated as the bending neutral axis). At each level of the imposed bending curvature, the potential energy of the filament is minimized, and its increase (per unit filament-length) relative to the potential energy of the straight filament is plotted as a function of the attendant curvature. Then the energy increase vs. curvature data are fitted using a quadratic functional relationship, in which the constant and the linear terms are set to zero, and the bending stiffness is set equal to the coefficient of the fitting function.

A similar procedure is applied to determine the axial stiffness of the actin filament, except that the filament is now subjected to axial/linear perturbations and the excess energy (for the entire filament) is plotted against the absolute value of the filament-length change. The axial stiffness is then set equal to the coefficient of the fitting quadratic function (analogous to the one described in the context of bending-stiffness determination).

It should be noted that actin-filament bending stiffness and axial stiffness quantify the mechanical response of actin filaments when these filaments are considered as discrete structural elements. As mentioned earlier, these quantities are used in structural-type analyses of the cell mechanical response. Often, however, cells are treated as a (heterogeneous) continuum and, in the continuum-type analyses, "*actin-material*" stiffness properties are required. Here, the term "*actin-material*" is used to denote an infinite-extent continuum consisting of randomly or irregularly arranged and solvated actin filaments. Determination of the effective actin-material stiffness properties is presented in the next section.

The bending-stiffness and the axial stiffness determination procedures described above are applied to both: (i) coarse-grained all-atom computational results; and (ii) coarse-grained computational-analyses results.

2.3.8. Actin-Material Visco-Elastic Properties

When the all-atom and/or coarse-grained MS and/or MD simulations are carried out under periodic boundary conditions, the results obtained can be used to compute the elements of the fourth-order elastic stiffness tensor or, equivalently, the components of the 6×6 elastic-stiffness matrix for the subject actin-based bulk material. These elastic-stiffness elements can be, in turn, post-processed using a homogenization procedure in order to compute the average isotropic elastic moduli. In the remainder of this section, a brief description is provided of the procedures which are used to extract the elastic-stiffness properties from either the molecular-statics or the molecular-dynamics all-atom/coarse-grained results.

2.3.8.1. Molecular-Statics-Based Elastic-Stiffness

As mentioned earlier, application of the molecular-statics procedure to an all-atom coarse-grained computational model places the system being analyzed into the condition of static equilibrium in which the forces acting on each particle are zero while the potential energy ($\boldsymbol{U}$) of the system is at its minimum. Elements of the fourth-order elastic-stiffness tensor can be determined by: (i) distorting the statically-equilibrated computational cell through the application of strains $\boldsymbol{\varepsilon_{ij}}$ and $\boldsymbol{\varepsilon_{kl}}$; (ii) application of the molecular-statics procedure to minimize the energy of the distorted unit cell; and (iii) using the resulting increase in the potential energy of the unit cell, within a finite-difference numerical scheme, to evaluate the second partial derivative of the system's potential energy with respect to the two components of strain in question about the system equilibrium as

$$c_{ijkl} = \frac{1}{V_0}\frac{\partial^2 U}{\partial \varepsilon_{ij}\partial \varepsilon_{kl}} \tag{10}$$

where V_0 is the equilibrated computational-cell volume, and the second partial derivative is obtained while keeping the remaining strain components unchanged.

The elements of the fourth-order elastic-stiffness tensor are next readily converted into their 6×6 elastic-stiffness matrix counterparts, $C_{\alpha\beta}$ (α, β = 1–6), using the Voigt conversion scheme [60]. Once the (anisotropic) elastic-stiffness constants $C_{\alpha\beta}$ are determined, they can be "*homogenized*" to obtain the effective isotropic stiffness moduli such as the Young's modulus (E), the shear modulus (G), the bulk modulus (K) or the Poisson's ratio (ν). There are several homogenization methods available such as the eigenstrain method developed by Eshelby [61] and Mora [62], effective medium theory [63], self-consistent method by Nemat-Nasser [64], etc. It should be noted that the elastic-stiffness constants/moduli obtained using the molecular-statics data pertain to the response of the subject material (actins, in the present case) at 0 K. To obtain the corresponding elastic-stiffness moduli at a finite temperature, molecular-dynamics results obtained at the temperature of interest should be used. Computation of the finite-temperature elastic-stiffness constants/moduli is discussed below.

2.3.8.2. Molecular-Dynamics-Based Elastic-Stiffness

Post-processing of the MD simulation results enables the computation of finite-temperature time-dependent elements of the fourth-order elastic-stiffness tensor, c_{ijkl} (t). This is done by employing the stress auto-correlation function,

$\left\langle \sigma_{ij}(0)\sigma_{kl}(t)\right\rangle$, as:

$$c_{ijkl}(t)=\frac{V}{k_BT}\left\langle \sigma_{ij}(0)\sigma_{kl}(t)\right\rangle \tag{11}$$

where k_B is the Boltzmann constant, T is the absolute temperature, and $\langle ... \rangle$ denotes ensemble average. As far as the components of the stress are concerned, they are computed using the virial theorem as

$$\sigma_{ij}=\frac{1}{V}\left[\sum_{I=1}^{n} m_I v_{Ii} v_{Ij}+\sum_{I=1}^{n-1}\sum_{J=I+1}^{n} r_{IJi}F_{IJj}\right] \tag{12}$$

where I and J denote atom/bead (not atom/bead-type) labels, n the total number of atoms/beads within the computational cell, v, r and F are atom/bead-velocity, inter-atom/bead position vector and inter-atom/bead force vectors, respectively. In Eq. (12), the first term on the right-hand side represents the dynamic (i.e. kinetic energy) contribution while the second term denotes the static (i.e. combined bonding and non-bonding energy) contribution to the stress. As discussed above, the elements of the fourth-order elastic-stiffness tensor can be readily converted into their corresponding elastic-stiffness matrix counterparts which, in turn, can be homogenized to obtain the corresponding isotropic elastic moduli.

In Eq. (11), the concept of stress auto-correlation function was used. To understand the concept of correlation functions, one should recognize the fact that (due to particle, i.e. atom or bead, interactions) particle trajectories are not completely independent during a MD simulation run. In other words, over a finite time period, particles tend to retain the memory of their initial (time=t_0) states (e.g. position, velocity, etc.). In the case of fluids, such memory becomes completely lost and the particles become uncorrelated (relative to t_0) after an infinite amount of time. In the case of solids, on the other hand, some particle correlation is retained indefinitely. To quantify the extent of particle correlations at an arbitrary time $t>t_0$, the time correlation functions (or simply correlation functions) are generally used. These functions quantify the correlation between two time-dependent material properties, $P(t)$ and $Q(t)$, as:

$$C(t)=\lim_{x\to\infty}\frac{1}{\tau}\int_0^x P(t_0)Q(t_0+t)\,dt_0 \tag{13}$$

When $P(t)$ and $Q(t)$ are different material properties, Eq. (13) defines a so-called "*cross-correlation*" function. Otherwise, application of this equation yields an "*auto-correlation*" function. It should be noted that the term τ in Eq. (13) is a normalization factor which ensures that the correlation function in question takes on a value of 1.0 at $t=t_0$.

2.3.8.3. Newtonian Shear Viscosity

To reveal the rate-dependent/dissipative behavior of the subject (actin-based) material, (Newtonian) shear viscosity η_s is computed from the time-dependent shear modulus $G(t)$ using the Green-Kubo formulation [65, 66] as:

$$\eta_s=\int_0^\infty G(t)dt \tag{14}$$

2.4. Problem Formulation

The two main problems addressed in the present work are as follows: (a) application of the computational methods and tools presented in Sections 2.1–2 in order to generate all-atom and coarse-grained trajectory data, and the utilization of the procedures described in Section 2.3 in order to determine various microstructural features and viscoelastic properties of the actin filaments; and (b) to validate the coarse-grained force-field functions derived, since future work involving larger actin-filament structures, as those encountered in smooth-muscle cell contractile elements, will be based on the use of c.g. computational methods and tools.

3. Results and Discussion

In this section, a brief description is provided of the results pertaining to various microstructural characteristics and properties of actin monomers, trimers and polymers, obtained in Section 2.3. In order to help relate the post-processing procedure(s) (as used) and the results obtained, the organization of the present section is analogous to that used in Section 2.3.

3.1. Topological Stability

Time-averaged α-carbon RMSDs for the cases of polymerized G-ATP and G-ADP are found to be 0.168 ± 0.005 and 0.191 ± 0.007 nm, respectively, relative to the corresponding time-averaged positions of the α-carbon atoms. This finding suggests that ATP hydrolysis and the accompanying dissociation of γ-phosphates causes a slight morphological destabilization of actin filaments. It should be noted that since the same all-atom RMSDs were used in the c.g. force-field parameterization procedure, the coarse-grained computational analyses are expected to reproduce these RMSDs (for the given type of nucleotide-bound actin). This was confirmed in the present work.

3.2. DNase I-Binding (DB) Loop Conformation

As mentioned earlier, DB-loop conformational changes are investigated by visually monitoring the temporal evolution of the α-carbon atoms residing within the residues constituting the DB loop. Unfortunately, within the computational times affordable in the present work, changes in the DB-loop conformation could not be observed, regardless of the character (ATP or ADP) of the

nucleotide which is bound to the G-actin. In other words, if the initial DB-loop conformation is of a loop type, the loop will retain this conformation, even in the case of G-ADP (the state of G-actin which is expected to be associated with the helical conformation of the DB loop). To obtain the helical conformation of the DB loop in this case, α-carbon atoms associated with the residues defining the DB-loop had to be manually perturbed into a helix-like configuration. Then, subsequent molecular-dynamics simulations assisted in formation of a more regular helix structure of the DB loop. An example of the results obtained after application of this procedure is displayed in Figures 3(a)–(d). It should be further noted that, since coarse-graining was carried out at the level of G-actin subdomains, c.g. computational methods could not be used to investigate DB-loop conformational changes.

3.3. G-actin Flatness

It should be recalled that the flatness of G-actin is assessed in the present work using two distinct methods: (a) via determination of the dihedral angle probability density function; and (b) via the use of the Ramachandran plots. In the remainder of this section, the corresponding two sets of results are presented and discussed.

The results obtained in the present work pertaining to the dihedral-angle distribution for the cases of polymerized ATP-bound G-actins with: (a) the loop-type; and (b) the helix-type conformation of the DB-loop are displayed in Figures 5(a)–(b), respectively. The corresponding results, but for the case of polymerized ADP-bound G-actins, are displayed in Figures 5(c)–(d), respectively. In each case, two sets of data are displayed, one obtained by coarse-graining all-atom trajectory data (the curves labeled "*All-Atom*"), and the other obtained using direct coarse-grained molecular-dynamics simulations (the curves labeled "*Coarse-Grained*"). Also, in each case, the values of the first four distribution moments are calculated. Examination of the results displayed in Figures 5(a)–(d) and the corresponding distribution-moment results reveals that:

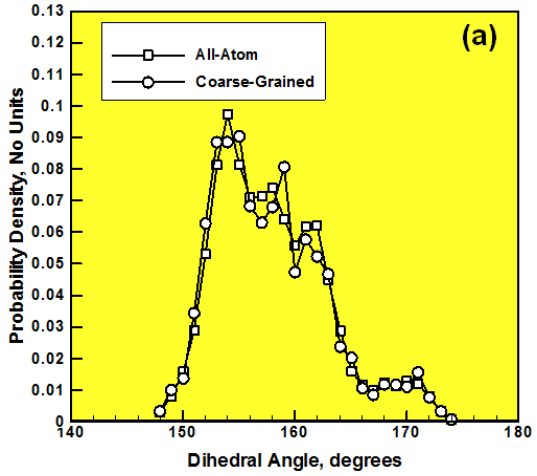

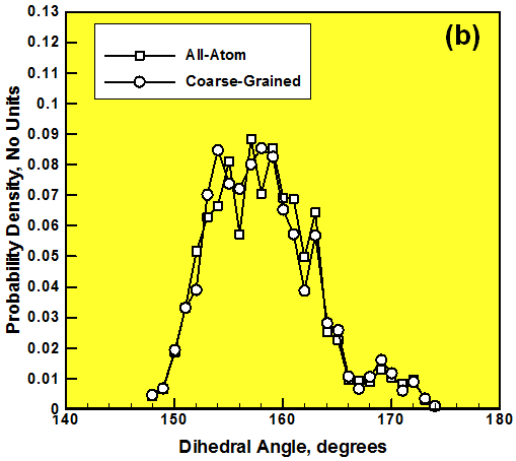

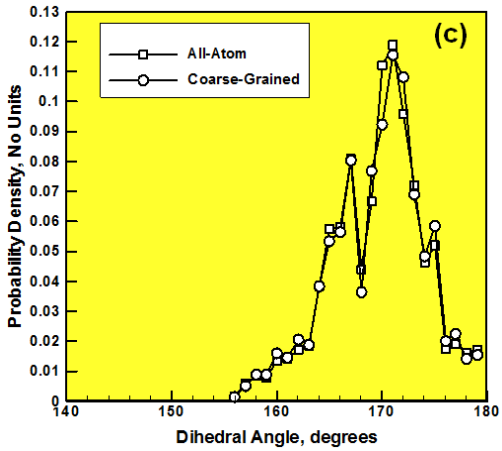

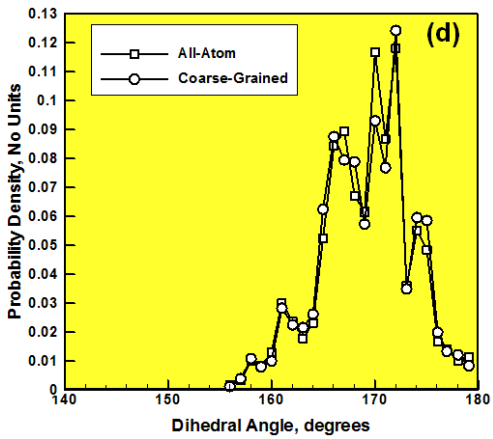

Figure 5. *All-atom and coarse-grained dihedral-angle probability distributions for the cases of: (a) ATP-bound G-actin with loop conformation of the DB-loop; (b) ATP-bound G-actin with helical conformation of the DB-loop; (c) ADP-bound G-actin with loop conformation of the DB-loop; and (d) ADP-bound G-actin with helical conformation of the DB-loop.*

(a) the all-atom and the corresponding coarse-grained results are generally in good agreement. For example, in the case of the ATP-bound G-actin with the loop conformation of the DB-loop, Figure 5(a), the mean, the standard deviation, the skewness and the kurtosis for the all-atom-/coarse-grained-based dihedral-angle distribution functions are: 158.0/157.9, 5.02/5.09, 0.701/0.740, and

0.176/0.196. Consequently, in the remainder of this section, only the all-atom-based results for different cases of G-actin-bound nucleotide and the DB-loop conformation will be discussed/compared;

(b) for the given bound-nucleotide, the DB-loop conformation has relatively little effect on the values of the dihedral-angle distribution function moments. For example, in the cases of the ATP-bound G-actin with the loop/helical conformation of the DB-loop, Figures 5(a)–(b), the mean, the standard deviation, the skewness and the kurtosis for the dihedral-angle distribution functions are: 158.0/158.3, 5.02/4.92, 0.701/0.559 and 0.176/0.182. Similarly, in the cases of the ADP-bound G-actin with the loop/helical conformation of the DB-loop, Figures 5(c)–(d), the mean, the standard deviation, the skewness and the kurtosis for the dihedral-angle distribution functions are: 169.6/169.1, 4.45/4.38, –0.367/–0.316 and 0.064/–0.046. One would generally expect that if the ATP-bound G-actin is assigned the higher-energy helical conformation DB-loop, it would spontaneously revert the DB-loop into its loop conformation. Likewise, one would expect that if the ADP-bound G-actin is assigned the higher-energy loop conformation DB-loop, it would spontaneously revert the DB-loop into its helical conformation. The fact that these transitions are not observed suggests that the associated activation energies are too high and/or the simulation times used are insufficiently long. Since the characteristic times for these transitions are expected to be on the order of seconds, the simulation times required for direct observation of the transitions are prohibitively long;

(c) the nature of the bound-nucleotide has the primary effect on the dihedral-angle distribution function within the polymerized G-actins. For example, in the cases of the ATP-/ADP-bound G-actins with the loop conformation of the DB-loop, Figures 5(a) and (c), the mean, the standard deviation, the skewness and the kurtosis for the dihedral-angle distribution functions are: 158.0/169.6, 5.02/4.45, 0.701/–0.367, 0.176/0.0644. This finding suggests that the ADP-bound G-actin is flatter, since a perfectly flat G-actin would have a dihedral angle of 180°; and

(d) while the changes in the bound-nucleotide type and the DB-loop conformation appear to significantly affect the values of skewness and kurtosis, on a relative scale, absolute values of these distribution moments are quite small, making physical interpretation of these changes difficult.

Examples of the Ramachandran plots for residues 142 and 337, obtained in the present work, are given in Figures 6(a)–(b), respectively. In each case, actin-polymer configurations based on both ATP-based loop and ADP-based helical conformation of the DNase I-binding loop are investigated. The results displayed in Figures 6(a)–(b) do not contain original scatter data but rather the corresponding mean values (shown as black-filled symbols) and one-standard-deviation domains of the two Ramachandran angles (shown as white-filled symbol-outlined ellipses). Examination of the results displayed in these figures shows that for the two conformations of the DNase I-binding loop, the distribution of the two Ramachandran angles are quite comparable in the case of residue 142. On the other hand, there is a distinct difference in the distributions of the Ramachandran angles for the two conformations of the DNase I-binding loop in the case of residue 337. This difference in distribution is an indication of the changes in the G-actin flatness accompanying actin polymerization and ATP hydrolysis. As a final remark, it should be noted that the Ramachandran plots are constructed using the G-actin backbone molecular-level structure and, hence, could not be generated using the coarse-grained representation of the G-actins.

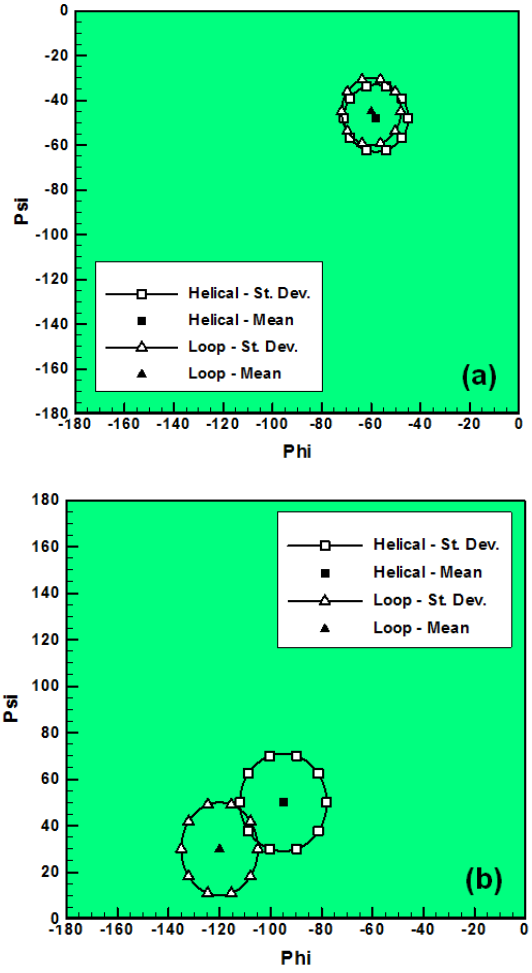

Figure 6. *Examples of the Ramachandran plots for residues (a) 142; and (b) 337. In each case, actin-polymer configurations based on both ATP-based loop and ADP-based helical conformation of the DNase I-binding loop are shown. Please see text for further explanation of the symbols.*

3.4. Conformation of Nucleotide-Binding Cleft

As mentioned earlier, the open/closed conformation of the nucleotide-binding cleft is investigated in the present work by monitoring the D2–D1–D3 and D1–D3–D4 bond angles. While one can determine the complete distribution function for each of these two angles, only the mean/equilibrium values and standard deviations of these

angles are monitored. Since the equilibrium values of these angles act as the c.g. force-field parameters, they were already computed using the procedure for coarse-graining the all-atom trajectory results. The results are shown in Tables 2 and 3. It should be noted that the use of coarse-grained simulation methods to re-compute these angles is not necessary since the results must be identical to their coarse-grained all-atom-data-based counterparts. Examination of the results shown in Tables 2 and 3 reveals that: (a) the nature of the nucleotide bound to the G-actin has relatively weak effect on the equilibrium values of the two bond angles. Specifically, for the case of the actin monomer, the ATP-bound configuration is associated with D2–D1–D3 angle of 95.9±0.4° while the ADP-bound configuration is associated with D2–D1–D3 angle of 95.9±0.2°; (b) the monomeric vs. polymeric environment of the G-actin only weakly affects the equilibrium values of the two bond angles, for both ATP-bound and ADP-bound configurations of the G-actins. However, the standard deviations take on significantly larger values in the polymerized form. For example, the ATP-bound monomeric form is associated with D1–D3–D4 bond angle of 93.3±0.15°, while the polymeric form is associated with D1–D3–D4 bond angle of 92.20±2.14°; and (c) despite the fact that the nature of the bound nucleotide affects the conformation of the DB loop, the nucleotide-binding cleft remains in the nearly-closed configuration (the configuration characterized by the D1–D3–D4 and D2–D1–D3 angles of approximately 90°).

3.5. Rate of ATP Hydrolysis

As mentioned earlier, polymerization of ATP-bound G-actin into actin filaments is accompanied by an increase in the rate of ATP hydrolysis by four orders of magnitude. This effect is often linked with the accompanying flattening of the G-actins [67], which positions the side-chain of the Q137 residue closer to the γ-phosphate group of the bound ATP. This conformational change is often assumed to be, at least partially, responsible for the observed increase in the rate of ATP hydrolysis in the actin filament relative to that in the monomeric G-actin. To establish the presence of this conformational change, all-atom computational results pertaining to the temporal evolution of the positions of the two hydrogen atoms in the NH_2 group of the Q137 side-chain, and the position of the oxygen atom bridging the terminal γ-phosphate and the adjacent β-phosphate are monitored. It was found that the mean distance between the hydrogen and oxygen atoms in question is smaller by 0.14 nm in the case of the flattened G-actin configuration. This finding confirms that the coordination between the Q137 side-group and the γ-phosphate is increased in the case of the ATP-bound, polymerized and flattened G-actins. However, direct all-atom computational investigations of the G-actin flattening process accompanying its polymerization, as mentioned earlier, is not feasible (due to prohibitively long simulation times required).

3.6. Filament Persistence-Length

The results of the aforementioned persistence-length calculation procedure are generally displayed using a plot of the natural logarithm of the cosine correlation function as a function of the contour distance. As mentioned above, the maximum value of the abscissa in such a plot is associated with a contour length (along the linearized chain) involving six adjacent bead/bead segments. An example of such a plot, obtained in the present work using coarse-grained all-atom computational results, showing the cosine correlation functions of the angles between tangent vectors as a function of the contour length, s, for the polymerized ATP-bound G-actin (termed F-ATP) and the polymerized ADP-bound G-actin (termed F-ADP), is depicted in Figure 7 [68]. According to Eq. (8), the natural logarithm of the θ-correlation function vs. s plot should be of a linear character and pass through the origin, while the negative slope of this plot should be equal to the reciprocal of the persistence length. Hence, to calculate the persistence length, the initial portion of the cosine-correlation function vs. contour-distance plot was first subjected to a linear regression analysis, under the constraints that the y-intercept is zero. Then, the persistence length is computed as the negative reciprocal of the resulting slope. To ensure sufficient accuracy of the computed persistence length, while conducting the linear regression analysis, the number of data points used (two in each case) is selected in such a way that the associated linear regression correlation coefficient R^2 has a value no less than 0.9.

Application of the aforementioned procedure to the (coarse-grained all-atom) / (coarse-grained molecular-analysis) data for the actin-filaments revealed that ATP hydrolysis (which results in the formation of ADP) and dissociation of γ-phosphate gives rise to a decrease in the filament persistence-length (from 15.9/16.6 μm in the case of F-ATP to 8.8/9.2 μm in the case of F-ADP), i.e. causes a reduction in actin-filament bending-stiffness.

3.7. Filament Bending Stiffness and Axial Stiffness

Application of the bending-stiffness determination procedure presented in Section 2.3.7 to the (coarse-grained all-atom)/(coarse-grained molecular-analysis) data for the actin-filaments revealed that ATP hydrolysis (which results in the formation of ADP) and dissociation of γ-phosphate indeed gives rise to a reduction in the filament bending stiffness (from 1.7 x 10^{-26}/1.6 x 10^{-26} Nm^2 in the case of F-ATP to 1.5 x 10^{-26} / 1.4 x 10^{-26} Nm^2 in the case of F-ADP). Furthermore, application of the axial-stiffness determination procedure presented in Section 2.3.7 to the (coarse-grained all-atom)/(coarse-grained molecular-analysis) data for the actin-filaments revealed that ATP hydrolysis also gives rise to a reduction in the filament axial stiffness (from 0.062±0.006/0.060±0.005 N/m in the case of F-ATP to 0.051±0.005/0.050±0.006 N in the case of F-ADP). These findings also confirm that the coarse-

grained force-field parameterization used can reasonably well account for the mechanical response of actin filaments when subjected to (small-deformation) bending and axial perturbations.

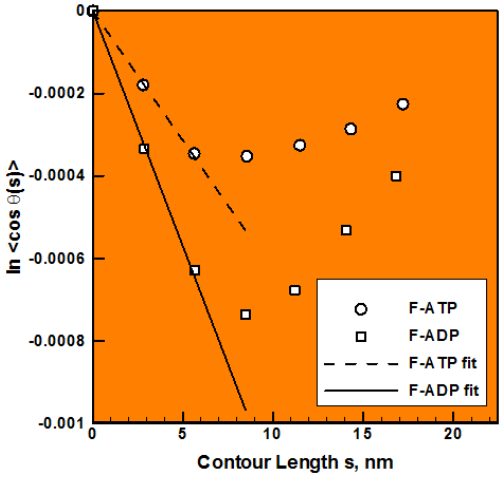

Figure 7. *Examples of the plots showing the cosine correlation functions of the angles between tangent vectors as a function of the contour length, s, and the corresponding straight lines obtained through linear regression of the initial few data points and used to determine the actin-filament persistence-length. Discrete points shown correspond to the coarse-grained all-atom data.*

3.8. Actin-Material Visco-Elastic Properties

3.8.1. Time-Dependent Isotropic Elastic Moduli

Since coarse-grained force-fields used in the present work do not include inter-filament interactions, while the same interactions exist within the all-atom computational framework (via the solvating water molecules and dissolved salts), one could not expect a good agreement between the elastic-stiffness results obtained using the two computational approaches. In addition, one should expect that the all-atom computational results (particularly those pertaining to the lateral response of the filaments) are more accurate/reliable. Consequently, the all-atom analyses-based results are presented first and in greater detail.

Temporal evolutions of the shear modulus for the actin-material based on the regularly-arranged parallel solvated ATP- and ADP-bound actin filaments are depicted in Figure 8(a). The corresponding results, but for the temporal evolutions of the bulk modulus, are depicted in Figure 8(b). The results displayed in these figures reveal that:

(a) for the most part, over the time range used, the values of the shear moduli are lower in the F-ADP than in the F-ATP case. This finding is consistent with the ones reported in the previous section pertaining to the actin-filament bending/axial stiffness;

(b) as far as the temporal evolution of the bulk modulus in F-ATP and F-ADP is concerned, it is more irregular in comparison to that of the shear modulus. In addition, the bulk modulus vs. time curves for the two actin-filament cases intersect multiple times, over the time range examined;

(c) at short times ($t < \sim 3 \times 10^{-4}$ ns), the rate of decrease of the given (shear or bulk) moduli for the two F-actin cases are quite comparable. This behavior could be readily explained considering the fact that, at short times, time-dependence of the shear and bulk moduli is controlled by bond-length adjustment/relaxation processes, the processes which are not expected to be significantly affected by the nature of the nucleotide bound to the polymerized G-actins;

(d) at intermediate times ($\sim 3 \times 10^{-4}$ ns $< t < \sim 2 \times 10^{-3}$ ns), relaxation of the two moduli in both actin-filament configurations acquires a nearly linear relationship in the log-log plots, Figures 8(a)–(b). It should be noted that this behavior for the shear modulus is consistent with the so-called Rouse scaling, which predicts that the slope of the suggested linear relationship between the logarithm of the modulus and the logarithm of the time should be –0.5. For the two actin-filament configurations analyzed in the present work, these shear-modulus vs. time slopes (on the log-log scale) are found to be quite similar (–0.475 for F-ATP and –0.479 for F-ADP) and very close to the Rouse value of –0.5. This finding is not surprising, considering the fact that actin filaments are all parallel and filament entanglement (typical source of the deviations from the Rouse behavior) is not feasible;

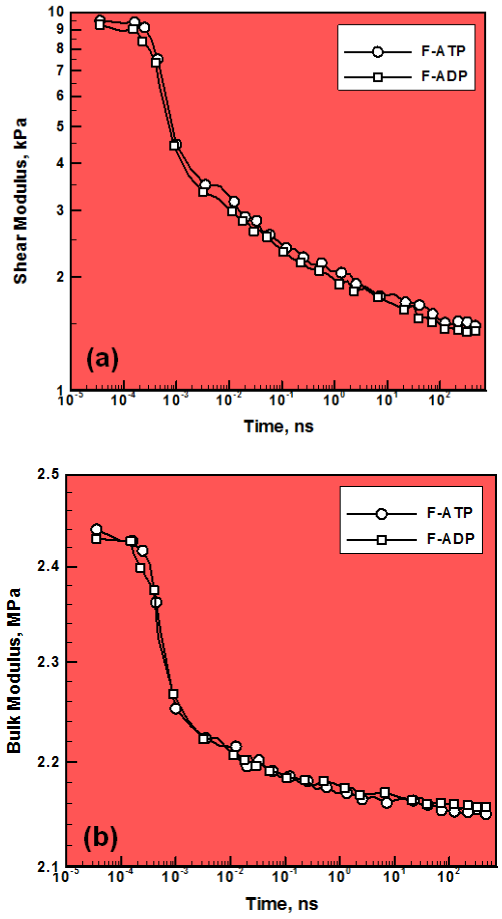

Figure 8. *Temporal evolution of (a) the shear and (b) the bulk moduli in the ATP-bound and ADP-bound states of actin filaments.*

(e) at the longest simulation times, each of the two moduli in both actin-filament configurations approaches a constant (bound-nucleotide dependent) value. This constant value could be considered as a long-term value of the corresponding modulus and is a measure of the time-independent/elastic response of the materials at hand; and

(f) values of the computed bulk modulus are comparable to the water bulk modulus of 2.2 GPa, which could be expected considering the fact that actin filaments analyzed are solvated in water.

As pointed out above, elastic-stiffness results based on the coarse-grained analysis data are not expected to be as accurate as their all-atom counterparts. Indeed, the coarse-grained results are found to be between 15–20% lower than their all-atom counterparts. It should be noted, however, that the results reported in this section were obtained under the assumption that the actin-material is isotropic. This approximation is not strictly valid, particularly in the present case, considering the fact that the actin filaments are all regularly arranged and parallel. Consequently, the resulting actin-material should be more properly described as an orthotropic (or, at least, transversely isotropic) material. When the actin-material was treated, in the present work, as an orthotropic material (detailed results not given for brevity), it was found that the values of the orthotropic Young's modulus associated with the filament axial direction obtained using all-atom and coarse-grained data, are within a few percent of each other. This finding suggests that coarse-grained force-field functions fairly accurately account for the observed axial response of the actin filaments, and could be used in the analyses which do not involve substantial lateral interactions between adjacent actin filaments.

3.8.2. Bulk and Shear Viscosities

Application of the viscosity-determination procedure, described in Section 2.3.8, to the all-atom computational results, yielded shear viscosity values of 4.73 mPa.s and 4.46 mPa.s for F-ATP and F-ADP, respectively. The corresponding results for the bulk viscosity are found to be 0.646 Pa.s and 0.644 Pa.s for F-ATP and F-ADP, respectively. These results suggest that ATP hydrolysis causes actin-material to become not only less compliant, as demonstrated above, but also to become less viscous (i.e. less time-dependent). Also, the shear viscosity results obtained in the present work are in general agreement with their experimental counterparts [69] (after account is taken of the differences in the molarity of the actin solutions in the two cases).

As mentioned above, stiffness, and thus, viscosity results based on the coarse-grained analysis data are less reliable and, thus, are not presented or discussed here.

4. Summary and Conclusions

Based on the results obtained in the present work, the following summary remarks and main conclusions can be drawn:

1. Various aspects of microstructure and properties in actin monomers and polymers are investigated using advanced computational methods and tools.
2. The specific aspects of actin microstructure and properties analyzed include: topological stability, DNase I-binding (DB) loop conformation, G-actin flatness, conformation of nucleotide-binding cleft, rate of ATP hydrolysis, filament persistence-length, filament bending stiffness and axial stiffness, and actin-material elastic-stiffness matrix/moduli.
3. During investigation of actin microstructure and properties, a combination of all-atom and coarse-grained molecular-level computational methods is used, along with a number of various coarse-graining and trajectory-data post-processing procedures.
4. To validate the computational approach used, the computed results are compared with their experimental counterparts.
5. Also, the coarse-grained force-field functions derived and parameterized in the present work are validated by demonstrating that predictions based on these functions are in reasonably good agreement with their counterparts based on the use of all-atom calculations.

Acknowledgements

A. G. would like to acknowledge the guidance and support of Professor Delphine Dean of the Department of Bioengineering at Clemson University.

References

[1] T. D. Pollard, L. Blanchoin and R. D. Mullins, "*Molecular mechanisms controlling actin filament dynamics in nonmuscle cells*," Annual Review of Biophysics and Biomolecular Structure, 29, 545–576, 2000.

[2] J. Howard, "*Mechanics of Motor Proteins and the Cytoskeleton*," Sinauer Associates, Sunderland, MA, 2001.

[3] E. D. Korn, "*Actin polymerization and its regulation by proteins from nonmuscle cells*," Physiol. Rev., 62, 672–737, 1982.

[4] P. Sheterline, J. Clayton and J. C. Sparrow, "*Actin*," Oxford University Press, New York, NY, 1998.

[5] J. A. Tuszynski, J. A. Brown and D. Sept, "*Models of the collective behavior of proteins in cells: tubulin, actin and motor proteins*," Journal of Biological Physics, 29, 401–428, 2003.

[6] A. Grujicic, M. Grujicic, J. S. Snipes, R. Galgalikar and S. Ramaswami, "*Material Modeling and Finite-Element Analysis of Active-Contractile and Passive Responses of Smooth Muscle Tissue*," Review of Bioinformatics and Biometrics, 2, 45–64, 2013.

[7] K. C. Holmes, D. Popp, W. Gebhard and W. Kabsch, "*Atomic structure of the actin: DNase I complex*," Nature, 347, 37–44, 1990.

[8] L. Blanchoin and T. D. Pollard, "*Hydrolysis of ATP by polymerized actin depends on the bound divalent cation but not profiling*," Biochemistry, 41, 597–602, 2002.

[9] M. A. Rould, Q. Wan, P. B. Joel, S. Lowey and K. M. Trybus, "*Crystal structures expressed nonpolymerizable monomeric actin in the ADP and ATP states*," Journal of Biological Chemistry, 281, 31909–31919, 2006.

[10] E. Reisler and E. H. Egelman, "*Actin's structure and function: what we still do not understand*," Journal of Biological Chemistry, 282, 36133–36137, 2007.

[11] P. Dalhaimer, T. D. Pollard and B. J. Nolen, "*Nucleotide-mediated conformational changes of monomeric actin and Arp3 studied by molecular dynamics simulations*," Journal of Molecular Biology, 376, 166–183, 2007.

[12] J. Pfaendtner, D. Branduardi, M. Parrinello, T. D. Pollard and G. A. Voth, "*Nucleotide-dependent conformational states of actin*," Proceedings of the National Academy of Sciences USA, 106, 12723–12728, 2009.

[13] J. Pfaendtner and G. A. Voth, "*Molecular dynamics simulation and coarse-grained analysis of the Arp2/3 complex*," Biophysical Journal, 95, 5324–5333, 2008.

[14] T. Oda, M. Iwasa, T. Aihara, Y. Maeda and A. Narita, "*The nature of the globular-to-fibrous-actin transition*," Nature, 457, 441–445, 2009.

[15] P. Graceffa and R. Dominguez, "*Crystal structure of monomeric actin in the ATP state*," Journal of Biological Chemistry, 278, 34172–34180, 2003.

[16] L. R. Otterbein, P. Graceffa and R. Dominguez, "*The crystal structure of uncomplexed actin in the ADP state*," Science, 293, 708–711, 2001.

[17] K. C. Holmes, D. Popp, W. Gebhard and W. Kabsch, "*Atomic model of the actin filament*," Nature, 347, 44–49, 1990.

[18] A. Orlova and E. H. Egelman, "*A Conformational Change in the Actin Subunit Can Change the Flexibility of the Actin Filament*," Journal of Molecular Biology, 232, 334–341, 1993.

[19] S. Y. Khaitlina, J. Moraczewska and H. Strzelecka-Golaszewska, "*The actin/actin interactions involving the N-terminus of the DNase-I-binding loop are crucial for stabilization of the actin filament*," European Journal of Biochemistry, 218, 911–920, 1993.

[20] E. Kim, M. Motoki, K. Seguro, A. Muhlrad and E. Reisler, "*Conformational changes in subdomain 2 of G-actin: fluorescence probing by dansyl ethylenediamine attached to Gln-41*," Biophysical Journal, 69, 2024–2032, 1995.

[21] A. Muhlrad, P. Cheung, B. C. Phan, C. Miller and E. Reisler, "*Dynamic properties of actin. Structural changes induced by beryllium fluoride*," Journal of Biological Chemistry, 269, 11852–11858, 1994.

[22] J. Moraczewska, H. Strzelecka-Golaszewska, P. D. J. Moens and C. G. dos Remedios, "*Structural changes in subdomain 2 of G-actin observed by fluorescence spectroscopy*," Biochemical Journal, 317, 605–611, 1996.

[23] Y. S. Borovikov, J. Moraczewska, M. I. Khoroshev and H. Strzelecka-Golaszewska, "*Proteolytic cleavage of actin within the DNase-I-binding loop changes the conformation of F-actin and its sensitivity to myosin binding*," Biochimica et Biophysica Acta, 1478, 138–151, 2000.

[24] A. Orlova and E. H. Egelman, "*Structural basis for the destabilization of F-actin by phosphate release following ATP hydrolysis,*"Journal of Molecular Biology, 227, 1043–1053, 1992.

[25] L. D. Belmont, A. Orlova, D. G. Drubin and E. H. Egelman, "*A change in actin conformation associated with filament instability after P_i release*," Proceedings of the National Academy of Sciences USA, 96, 29–34, 1999.

[26] S. B. Smith, L. Finzi and C. Bustamante, "*Direct mechanical measurements of the elasticity of single DNA molecules by using magnetic beads*," Science, 258, 1122–1126, 1992.

[27] T. R. Strick, J.-F. Allemand, D. Bensimon, A. Bensimon and V. Croquette, "*The elasticity of a single supercoiled DNA molecule*," Science, 271, 1835–1837, 1996.

[28] S. Panyukov and Y. Rabin, "*Thermal Fluctuations of Elastic Filaments with Spontaneous Curvature and Torsion*," Physical Review Letters, 85, 2404–2407, 2000.

[29] S. Panyukov and Y. Rabin, "*Fluctuating filaments: statistical mechanics of helices*," Physical Review E, 62, 7135–7146, 2000.

[30] A. D. MacKerell, D. Bashford, M. Bellott, R. L. Dunbrack, J. D. Evanseck, M. J. Field, S. Fischer, J. Gao, H. Guo, S. Ha, *et al*, "*All-Atom Empirical Potential for Molecular Modeling and Dynamics Studies of Proteins*," Journal of Physical Chemistry B, 102, 3586–3616, 1998.

[31] B. R. Brooks, R. E. Bruccoleri, B. D. Olafson, , D. J. States, S. Swaminathan and M. Karplus, "*CHARMM: A program for macromolecular energy, minimization, and dynamics calculations*," Journal of Computational Chemistry, 4, 187–217, 1983.

[32] M. P. Allen and D. J. Tildesley, "*Computer Simulation of Liquids*," Oxford University Press, New York, 1987.

[33] J.-W. Chu and G. A. Voth, "*Allostery of actin filaments: Molecular dynamics simulations and coarse-grained analysis*," Proceedings of the National Academy of Sciences USA, 102, 13111–13116, 2005.

[34] E. Andrianantoandro, L. Blanchoin, D. Sept, J. A. McCammon and T. D. Pollard, "*Kinetic mechanism of end-to-end annealing of actin filaments*," *Journal of Molecular Biology*, 312, 721–730, 2001.

[35] D. Sept, J. Y. Xu, T. D. Pollard and J. A. McCammon, "*Annealing accounts for the length of actin filaments formed by spontaneous polymerization*," Biophysical Journal, 77, 2911–2919, 1999.

[36] R. Goetz and R. Lipowsky. "*Computer simulations of bilayer membranes: self-assembly and interfacial tension*," Journal of Chemical Physics 108, 7397–7409, 1998.

[37] S. J. Marrink and A. E. Mark, "*Molecular dynamics simulation of the formation, structure, and dynamics of small phospholipid vesicles*," Journal of the American Chemical Society, 125, 15233–15242, 2003.

[38] J. C. Shelley and M. Y. Shelley, "*Computer simulation of*

surfactant solutions," Current Opinions in Colloid and Interface Science, 5, 101–110, 2000.

[39] B. Smit, K. Esselink, P. A. Hilbers, N. M. van Os, L. A. M. Rupert and I. Szleifer, "*Computer simulations of surfactant self-assembly*," Langmuir, 9, 9–11, 1993.

[40] J.-W. Chu and G. A. Voth, "*Coarse-Grained Modeling of the Actin Filament Derived from Atomistic-Scale Simulations*," Biophysical Journal, 90, 1572–1582, 2006.

[41] M. M. Tirion, "*Large amplitude elastic motions in proteins from a single parameter, atomic analysis*," Physical Review Letters 77, 1905–1908, 1996.

[42] T. Halioglu, I. Bahar and B. Erman, "*Gaussian dynamics of folded proteins*," Physical Review Letters 79, 3090–3093, 1997.

[43] I. Bahar and R. L. Jernigan, "*Vibrational dynamics of transfer RNAs: comparison of the free and synthetase-bound forms*," Journal of Molecular Biology, 281, 871–884, 1998.

[44] M. Delarue and Y. H. Sanejouand, "*Simplified normal mode analysis of conformational transitions in DNA-dependent polymerases: the elastic network model*," Journal of Molecular Biology, 320, 1011–1024, 2002.

[45] W. J. Zheng and S. Doniach, "*A comparative study of motor protein motions by using a simple elastic-network model*," Proceedings of the National Academy of Sciences USA, 100, 13253–13258, 2003.

[46] W. J. Zheng and B. Brooks, "*Identification of dynamical correlations within the myosin motor domain by the normal mode analysis of an elastic network model*," Journal of Molecular Biology, 346, 745–759, 2005.

[47] M. M. Tirion, D. Benavraham, M. Lorenz and K. C. Holmes, "*Normal-modes as refinement parameters for the F-actin model*," Biophysical Journal, 68, 5–12, 1995.

[48] Visualizer, http://www.accelrys.com/mstudio/ms modeling/visualiser.html, accessed on accessed on Apr 21, 2013.

[49] Matlab, http://www.mathworks.com, accessed on May 3, 2013.

[50] PDB, http://www.rcsb.org/pdb, accessed on May 3, 2013.

[51] W. L. Jorgensen, J. Chandrasekhar, J. D. Madura, R. W. Impey and M. L. Klein, "*Comparison of simple potential functions for simulating liquid water*," Journal of Chemical Physics, 79, 926–935, 1983.

[52] W.R.P. Scott, P.H. Huenenberger, I.G. Tironi, A.E. Mark, S.R. Billeter, J. Fennen, A.E. Torda, T. Huber, P. Krueger and W.F. van Gunsteren, "*The GROMOS Biomolecular Simulation Program Package*," Journal of Physical Chemistry A, 103, 3596–3607, 1999.

[53] T. Schlick, "*Molecular Modeling and Simulation: an Interdisciplinary Guide*," Interdisciplinary Applied Mathematics, Mathematical Biology, Vol. 21, Springer-Verlag: New York, NY, 2002.

[54] H. J. C. Berendsen, D. van der Spoel and R. van Drunen, "*GROMACS: A message-passing parallel molecular-dynamics implementation*," Computer Physics Communications, 91, 43–56, 1995.

[55] L. Verlet, "*Computer 'experiments' on classical fluids. I. Thermodynamical properties of Lennard-Jones molecules*," Physical Review, 159, 98–103, 1967.

[56] M. P. Allen and D. J. Tildesley, "*Computer Simulation of Liquids*," Oxford Univ. Press, New York, 1987.

[57] Discover, http://www.accelrys.com/mstudio/ms modeling/discover.html

[58] J. F. Marko and E. D. Siggia, "*Stretching DNA*," Macromolecules, 28, 8759–8770, 1995.

[59] B. R. Brooks, D. Janezic and M. Karplus, "*Harmonic analysis of large systems. I. Methodology*," Journal of Computational Chemistry, 16, 1522–1542, 1995.

[60] S. Timoshenko and J. N. Goodier, "*Theory of Elastic Stability, 2nd Ed.,*" McGraw-Hill: Columbus, OH, 1951.

[61] J. D. Eshelby, "*The determination of the elastic field of an ellipsoidal inclusion, and related problems*," Proceedings of the Royal Society of London A, 241, 376–396, 1957.

[62] T. Mura, "*Micromechanics of Defects in Solids*," Kluwer: Dordrecht, Germany, 1987.

[63] Tuck C. Choy, "*Effective Medium Theory: Principles and Applications (International Series of Monographs on Physics (Oxford, England), 102)*," Oxford University Press (Sd)., 1999

[64] S. Nemat-Nasser and M. Hori, "*Micromechanics: Overall Properties of Heterogeneous Materials (North Holland Series in Applied Mathematics and Mechanics)*," Elsevier: New York, NY, 1993.

[65] M. S. Green, "*Markoff Random Processes and the Statistical Mechanics of Time-Dependent Phenomena. II. Irreversible Processes in Fluids*," Journal of Chemical Physics, 22, 398–413, 1954.

[66] R. Kubo, "*Statistical-Mechanical Theory of Irreversible Processes. I. General Theory and Simple Applications to Magnetic and Conduction Problems*," Journal of the Physical Society of Japan, 12, 570–586, 1957.

[67] M. Iwasa, K. Maeda, A. Narita, Y. Maéda and T. Oda, "*Dual roles of Gln137 of actin revealed by recombinant human cardiac muscle alpha-actin mutants*," Journal of Biological Chemistry, 283, 21045–22103, 2008.

[68] H. Isambert, P. Venier, A. C. Maggs, A. Fattoum, R. Kassab, D. Pantaloni and M. F. Carlier, "*Flexibility of actin filaments derived from thermal fluctuations. Effect of bound nucleotide, phalloidin, and muscle regulatory proteins*," Journal of Biological Chemistry, 270, 11437–11444, 1995.

[69] H. Lee, J. M. Ferrer, F. Nakamura, M. J. Lang and R. D. Kamma, "*Passive and active microrheology for cross-linked F-actin networks in vitro*," Acta Biomaterialia, 6, 1207–1218, 2010.